



DEPARTMENT OF
PHYSICS

PEDRO DAVID ARSÉNIO COPETO

BSc in Physics Engineering

LIGHT FRAGMENT DETECTION USING RESISTIVE PLATE CHAMBERS

CONTRIBUTION TO GSI EXPERIMENT G249

MASTER IN PHYSICS ENGINEERING

NOVA University Lisbon

Draft: September 1, 2025

LIGHT FRAGMENT DETECTION USING RESISTIVE PLATE CHAMBERS

CONTRIBUTION TO GSI EXPERIMENT G249

PEDRO DAVID ARSÉNIO COPETO

BSc in Physics Engineering

Adviser: Daniel Galaviz Redondo

Assistant Professor, University of Lisbon

Co-advisers: João Duarte Neves Cruz

Associate Professor, NOVA University Lisbon

John Doe other Co-Adviser Name

Full Professor, NOVA University Lisbon

ABSTRACT

This will be my abstract.

Keywords: Resistive plate chamber, Quasi-free scattering, Gaseous detectors, One keyword more, The last keyword

RESUMO

Este vai ser o meu resumo.

Palavras-chave: Câmara de placas resistivas, Dispersão quase livre, Detetores gasosos, A última palavra-chave

CONTENTS

List of Figures	v
Acronyms	vii
1 Introduction	1
1.1 Introduction	1
1.1.1 The Liquid-drop Model	2
1.1.2 The Shell Model	2
1.1.3 Conclusion	4
1.2 The FAIR Facility	4
1.3 Author’s Contribution and Thesis Overview	6
2 Direct Reactions as Spectroscopic Tools	7
2.1 Introduction	7
2.2 Transfer Reactions	7
2.3 Knockout Reactions	8
2.4 From Knockout to Quasi-Free Scattering	8
2.5 Quasi-free Scattering Reactions	9
2.5.1 Introduction to Quasi-Free Scattering	9
2.5.2 Historical Context and the Electron-Induced Paradigm	9
2.5.3 Proton-Induced QFS and DWIA Evolution	10
2.5.4 The Modern Era: Inverse Kinematics and Exotic Nuclei	10
2.5.5 Benchmark and Current Frontiers	11
3 Experiment	12
3.1 Context and Goal of the Experiment	12
3.2 The GSI Accelerator System	13
3.2.1 From Source to Experimental Cave	13
3.2.2 Beam used in Experiment	17
3.3 R ³ B Setup	18

3.3.1	Role of each detector	20
3.3.2	Main DAQ	22
3.4	Personal Contribution to the Experiment	22
4	RPC	23
4.1	Introduction and Historical Context	23
4.2	Detector Design, Construction, and Properties	24
4.3	Operating Principle and Gas System	25
4.3.1	Gas Mixture and Physics Motivation	25
4.3.2	Operating Pressure	26
4.3.3	Detector Operating Modes	26
4.4	Readout Electronics and Signal Reconstruction	27
4.5	Performance in Previous Beam Time	28
4.6	Role of the RPC in the Present Experiment	28
4.7	Detector Preparation Procedure	28
4.8	Contributions to Detector Operation and Monitoring	30
4.8.1	Monitoring Infrastructure for RPC Voltage and Current	30
4.8.2	Remote Control and Recovery Tools	31
5	Simulation and Analysis	32
5.1	Geant4	33
5.2	ROOT	33
5.3	R3BRoot	33
5.4	Plots	33
5.5	Multidimensional Fitting	33
5.5.1	Application to the RPC and FOOT Detectors	34
5.5.2	Validation of the MDF Models	35
5.6	Conclusions for the Experiment	35
6	Results	36
	Bibliography	37
	Appendices	
A	RPC Plots	44
	Annexes	
I	GSI Accelerator Facility	45

LIST OF FIGURES

1.1	Single-particle shell model level scheme illustrating the origin of nuclear magic numbers after incorporating spin-orbit coupling. The diagram shows the energy splitting of nuclear orbitals due to spin-orbit interaction, leading to the observed magic numbers (circled) corresponding to closed shells at nucleon numbers 2, 8, 20, 28, 50, 82, 126, and 184. The levels are labeled with their orbital and total angular momentum quantum numbers nlj , and the associated degeneracy $(2j+1)$ is indicated on the right. Reprinted figure from Ref. [9]	3
1.2	Layout of GSI-FAIR with the existing and planned beamlines shown in blue and red, respectively. The experimental sites are marked in black (figure: GSI Darmstadt). © Copyright: GSI/FAIR.	5
2.1	Schematic diagram of a QFS reaction induced by a proton p^+ on a nucleus A via elastic scattering off the virtual constituent particle X^* . Three real particles are generated in the final state: the scattered proton p^+ , the knock-out cluster X and the spectator nuclear fragment $(A-X^*)$. Reprinted figure from Ref. [24]	10
3.1	Visualization of the neutron drip line extension from oxygen to fluorine. The extended neutron-rich limit for fluorine isotopes illustrates how additional protons influence nuclear binding near the drip line. Figure adapted from the IAEA Live Chart of Nuclides [36].	13
3.2	Schematic layout of the GSI Helmholtzzentrum accelerator facility. The diagram shows the major components including the ion sources, the UNILAC linear accelerator, the SIS18 synchrotron, the Fragment Separator (FRS), and the associated experimental halls [37].	14
3.3	Detailed schematic of the UNILAC accelerator. The figure highlights the beamline structure from ion sources through the High Current Injector (HSI), Radio-Frequency Quadrupole (RFQ), Interdigital H-mode Drift Tube Linacs (IH-DTL), gas stripper section, Alvarez Drift Tube Linac (DTL), and the transfer line to SIS18. Beam diagnostic and stripping sections are also labeled [40].	15

3.4	Plan view of the SIS18 heavy-ion synchrotron, illustrating its 12 identical lattice sections, dipole and quadrupole magnet configurations, RF acceleration cavities, and positions of beam diagnostic systems [42].	15
3.5	Schematic of the FRS system showing its dipole magnet sections, dispersive and achromatic focal planes (F1–F8), and the separation of rare isotope beams. The figure also shows the branching to dedicated experimental areas, including the Direct Branch, Ring Branch (ESR), and the experimental caves [44]. . . .	16
3.6	Layout of GSI-FAIR with Cave C highlighted, where the prototype of the future NUSTAR R ³ B setup stands and where the present experiment took place. .	17
3.7	Expected secondary cocktail beam of ²⁵ F in Cave C as obtained by LISE++ calculations. The numbers under the names of isotopes indicate calculated rates per second. Reprinted figure from Ref. [31].	18
3.8	Sketch of the experimental setup at R ³ B.	19
4.1	Schematic representation of the top view of the RPC. Reprinted from [50]. .	25
4.2	Measured strip efficiency of the RPC during beam time.	28
4.3	Calibration of the RPC working point using cosmic ray data. The top-left panel shows the distribution of events as a function of the mean position on the scintillators for different applied voltages. The top-right panel presents the corresponding efficiency curves as a function of position for four high-voltage settings (7500, 7750, 8000, and 8250 V). The bottom-left panel shows the time-over-threshold (ToT) distributions for the same voltages, which are used as a quality criterion for hit selection. The bottom-right panel summarizes the overall efficiency as a function of the applied voltage, including results from previous beam campaigns for comparison.	30
4.4	Example of live Grafana dashboard showing voltage and current monitoring of the RPC during beam operation.	31
5.1	Example of an event in a simulation. In this case, there's a ¹⁴ C passing through ToFD, a Deuteron passing through the RPC and 3 neutrons going to NeuLAND.	32

ACRONYMS

- DAQ** Data Acquisition (*p.* [22](#))
- FAIR** Facility for Antiproton and Ion Research (*pp.* [4–6](#), [16](#), [28](#))
- FRS** FRagment Separator (*pp.* [14](#), [16](#), [17](#))
- QFS** Quasi-free Scattering (*pp.* [9–12](#))
- R³B** Reactions with Relativistic Radioactive Beams (*pp.* [6](#), [12](#), [13](#), [16](#), [18](#), [20](#), [24](#), [27](#), [28](#), [32–35](#))
- RPC** Resistive Plate Chamber (*pp.* [24–31](#), [33](#), [34](#))

INTRODUCTION

"The important thing in science is not so much to obtain new facts as to discover new ways of thinking about them."

Sir William Lawrence Bragg

1.1 Introduction

Since the birth of Nuclear Physics, with the discovery of the atomic nucleus by Ernest Rutherford in 1911 [1], this area has proved to be a fascinating field for scientific research displaying a rich variety of quantum phenomena. Many features of the nucleons in the nucleus exhibited are similar to the structure and behavior of atomic electrons in the atom. Similar descriptions for energy levels and shells, spins and angular momentum have emerged.

But there are some differences:

1. The dominating force inside the nucleus is the strong force rather than the electromagnetic one.
2. Since the strong force is short range and attractive, the potential in which the nucleons exist is created by all the other nucleons in contrast to the force between the atomic electrons and the spatially separated positive charge of the nucleus.

Two fundamental models—the liquid-drop model and the shell model—represent key milestones in the development of understanding the nucleus. Their reconciliation explains many nuclear phenomena, particularly the emergence of magic numbers and the behavior of exotic nuclei.

1.1.1 The Liquid-drop Model

The liquid-drop model, first formulated comprehensively by Weizsäcker [2] and discussed in detail by Bethe and Bacher in 1936 [3], treats the nucleus analogously to a charged droplet of incompressible fluid. This model emphasizes collective properties of the nucleus, such as binding energy, surface tension, and Coulomb repulsion among protons.

The semi-empirical mass formula (also called the Bethe-Weizsäcker formula) captures essential trends:

$$B(A, Z) = a_V A - a_S A^{2/3} - a_C \frac{Z(Z-1)}{A^{1/3}} - a_A \frac{(N-Z)^2}{A} \pm \delta(N, Z)$$

where each term accounts for volume, surface, Coulomb, asymmetry, and pairing effects respectively.

While successful at explaining global nuclear properties—such as the approximate binding energy per nucleon—it could not account for observed anomalies in nuclear stability, such as nuclei at specific nucleon numbers (2, 8, 20, 28, 50, 82, 126) exhibiting enhanced stability: the magic numbers.

1.1.2 The Shell Model

The limitations of the liquid-drop model led to the proposal of the nuclear shell model, developed independently by Maria Goeppert Mayer [4] and by Haxel, Jensen, and Suess [5] in the late 1940s. Mayer and Jensen later collaborated on a comprehensive treatment of the model [6], and were jointly awarded the Nobel Prize in Physics in 1963 for their contributions. Their work, expanding on the early suggestions of Elsasser [7], showed that nucleons move in quantized energy levels within a mean potential well created by all other nucleons—analogueous to electrons in atomic orbitals.

Initially, it was thought that a simple three-dimensional harmonic oscillator potential could describe the structure. However, it was soon realized that including a strong spin-orbit coupling term, where the nucleon's spin couples to its orbital motion, was critical to reproduce the magic numbers observed experimentally [8].

In particular, spin-orbit splitting lifts the degeneracy of orbital states, energetically favoring high-angular-momentum states (e.g., $j = l + 1/2$), thus producing large energy gaps at specific nucleon numbers—those corresponding to the magic numbers. This effect is illustrated in Figure 1.1, which shows the rearrangement of single-particle levels and the resulting magic numbers emerging from spin-orbit coupling.

The modified energy level filling, based on this strong spin-orbit interaction, led to a successful explanation for the pronounced nuclear stability at nucleon numbers:

$$2, 8, 20, 28, 50, 82, 126$$

for both protons and neutrons separately [8].

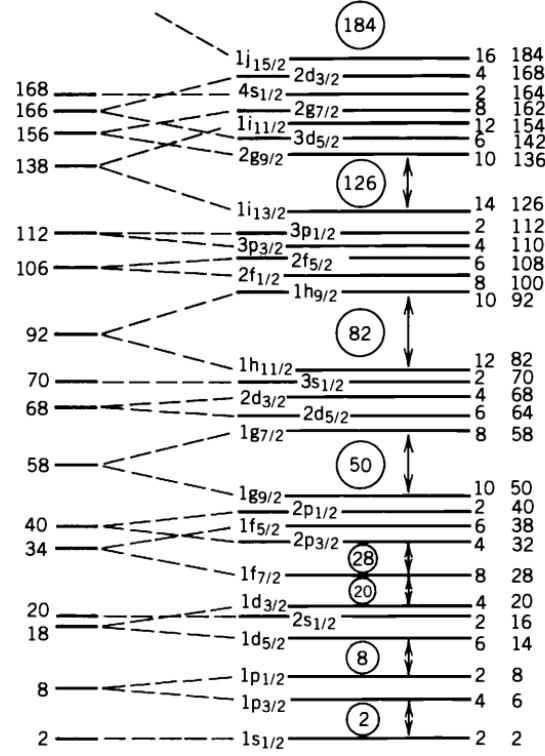


Figure 1.1: Single-particle shell model level scheme illustrating the origin of nuclear magic numbers after incorporating spin-orbit coupling. The diagram shows the energy splitting of nuclear orbitals due to spin-orbit interaction, leading to the observed magic numbers (circled) corresponding to closed shells at nucleon numbers 2, 8, 20, 28, 50, 82, 126, and 184. The levels are labeled with their orbital and total angular momentum quantum numbers nlj , and the associated degeneracy $(2j+1)$ is indicated on the right. Reprinted figure from Ref. [9]

1.1.2.1 Magic Numbers and Shell Closures

In the shell model:

- A closed shell means that all available states at a given energy are filled.
- Nuclei with both proton and neutron numbers equal to magic numbers (so-called doubly magic nuclei, e.g., ^{16}O , ^{208}Pb) exhibit especially high binding energies, spherical shapes, and relatively low excitation spectra.

Haxel, Jensen, and Suess [5] provided a succinct explanation showing how a strong spin-orbit coupling splits the energy levels such that filling up the states naturally reproduces the magic numbers.

1.1.2.2 Extension to Exotic Nuclei

The classic shell model was originally built based on stable and near- β -stable nuclei. However, advances in experimental techniques have allowed the study of exotic nuclei—nuclei far from stability, with unusual neutron-to-proton ratios.

In these systems traditional magic numbers can weaken or even disappear, new magic numbers (e.g., $N = 16$, $N = 34$) can emerge, nuclear deformations become more common, especially near the so-called "island of inversion" (around $N = 20$) and phenomena like neutron halos emerge [10].

This phenomena has led to the concept of shell evolution, where the shell structure depends on the balance between the nuclear force components (central, spin-orbit, and tensor interactions) and changes with proton-neutron ratios.

1.1.3 Conclusion

In summary, the liquid-drop model offered a macroscopic view of nuclear behavior, while the shell model introduced microscopic structure and quantization effects that explain nuclear stability at magic numbers. The discovery of exotic nuclei has highlighted that the shell structure itself is dynamic and evolves under extreme conditions, demonstrating the richness and complexity of nuclear structure beyond the stable valley.

The quest for obtaining a model that will adequately describe the nucleus in all areas of stability, as well as at the extremes of nuclear existence has been motivating the last 60 years of nuclear physics and has led to the designing of new laboratories, such as the FAIR facility.

1.2 The FAIR Facility

The Facility for Antiproton and Ion Research (FAIR), currently under construction as an expansion to the existing GSI¹ in Darmstadt, Germany, represents one of the most ambitious research infrastructures worldwide for exploring the structure of matter and the evolution of the universe. FAIR will provide intense, high-quality beams of protons, antiprotons, and ions—ranging from hydrogen to uranium—enabling unique access to a wide range of unexplored regimes in hadronic, nuclear, atomic, and plasma physics, as well as interdisciplinary and applied sciences.

The FAIR accelerator complex, seen in Figure 1.2, is centered around the superconducting synchrotron SIS100 [11], which, with its 100 Tm magnetic rigidity and 1100 m circumference, will serve as the backbone for beam delivery. The accelerator system is complemented by specialized storage rings and the Super-FRS fragment separator [12], facilitating the production and manipulation of both stable and exotic radioactive beams with intensities and purities that exceed those of existing facilities by several orders of magnitude.

¹GSI Helmholtzzentrum für Schwerionenforschung

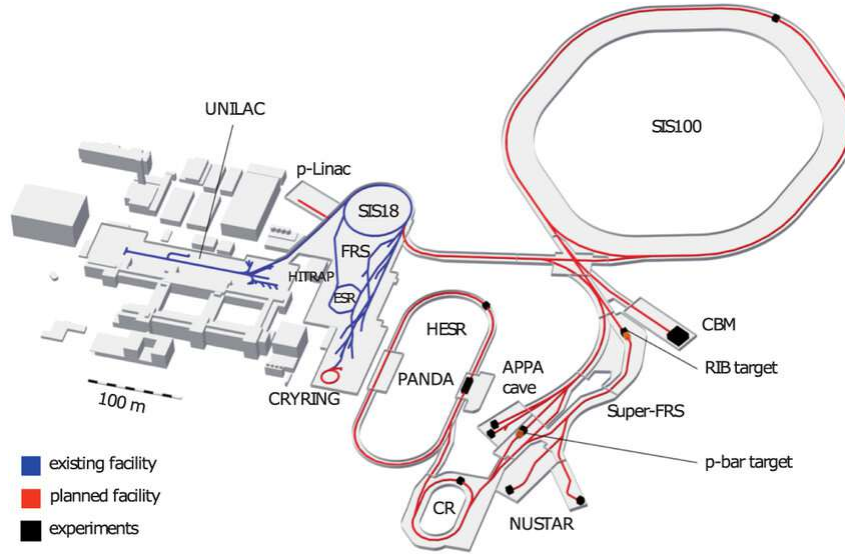


Figure 1.2: Layout of GSI-FAIR with the existing and planned beamlines shown in blue and red, respectively. The experimental sites are marked in black (figure: GSI Darmstadt). © Copyright: GSI/FAIR.

FAIR's scientific program is structured around four foundational experimental pillars [13–15]:

- APPA – Atomic Physics, Plasma Physics, and Applications [16]

The APPA collaboration focuses on high-precision studies in atomic and plasma physics, particularly utilizing highly charged ions and high-intensity ion beams. This enables research into correlated electron dynamics under ultra-strong electromagnetic fields, tests of quantum electrodynamics (QED) in critical regimes, and the investigation of high energy density matter relevant to astrophysical phenomena and fusion technologies. APPA also addresses applied sciences such as materials modification and radiation biology under cosmic-ray-like ion bombardment.

- CBM – Compressed Baryonic Matter [17]

The CBM experiment aims to map the QCD phase diagram at high baryon densities and moderate temperatures, a region largely inaccessible to collider experiments like those at RHIC and LHC. Using high-intensity heavy-ion beams from SIS100, CBM will explore the properties of dense nuclear matter, the nuclear equation of state, and search for signals of deconfinement, chiral symmetry restoration, and the QCD critical point. It features the measurement of rare probes such as dileptons, open and hidden charm, and multi-strange hyperons with unprecedented statistics.

- PANDA – AntiProton ANnihilation at DArmstadt [18]

PANDA will utilize antiproton beams stored and cooled in the High Energy Storage Ring (HESR) to investigate the structure of hadrons and their interactions. Its focus

includes charmonium spectroscopy, the identification of exotic states such as hybrids and glueballs, and studies of the hadron mass generation mechanism via gluonic dynamics. PANDA's precision measurements are expected to yield insights into the strong force at the confinement scale, extending beyond the capabilities of previous antiproton experiments.

- NuSTAR – Nuclear Structure, Astrophysics, and Reactions [19]

The NuSTAR collaboration (Nuclear Structure, Astrophysics and Reactions) lies at the heart of FAIR's mission to investigate nuclei far from stability and their relevance in cosmic nucleosynthesis. NuSTAR's scientific objectives include exploring the structure of nuclei near the drip lines, understanding the processes driving the astrophysical r-process, and studying fundamental interactions and symmetries through decay modes and reaction dynamics of exotic nuclei.

Central to NuSTAR is the Super-FRS, a high-resolution, multi-stage fragment separator designed to deliver intense, isotope-pure beams of radioactive ions. These beams will allow exploration of previously inaccessible regions of the nuclear chart. A vital component of NuSTAR is the Reactions with Relativistic Radioactive Beams (R³B) collaboration, which is dedicated to reaction studies in inverse kinematics using high-energy exotic nuclei. R³B will enable kinematically complete measurements of a wide variety of reaction channels (e.g., knockout, breakup, Coulomb excitation), providing deep insights into nuclear forces, shell evolution, and exotic decay modes. The R³B setup combines active and passive detectors in a versatile setup optimized for the coincident detection of charged particles, neutrons, and γ -rays.

1.3 Author's Contribution and Thesis Overview

Simulations for the experiment.

RPC preparation: Moved NeuLAND bar for calibration. Flashed RPC and inserted the gas mixture. Found working point.

Developed a script to monitor voltage and current in the RPC resistive plates.

Updated a script to power cycle RPC and reboot DAQ and Acquisition.

Developed MDF functions for PID in RPC.

DIRECT REACTIONS AS SPECTROSCOPIC TOOLS

"The art of simplicity is a puzzle of complexity."

Douglas Horton

2.1 Introduction

The structure of atomic nuclei—how protons and neutrons arrange themselves in shells, how they correlate, and how these features evolve across the nuclear chart—has been at the heart of nuclear physics for decades. To unravel this structure, nuclear physicists have long relied on direct reaction mechanisms, in which a projectile interacts with a target nucleus in a controlled and selective way, producing clean signatures of specific internal configurations. Among these, transfer reactions and knockout reactions have historically provided the foundational experimental pathways for exploring the single-particle nature of the nucleus.

2.2 Transfer Reactions

Nucleon transfer reactions, such as (d,p) , (p,d) , or (t,α) , involve the exchange of one or more nucleons between the projectile and the target. In the classic (d,p) reaction, for instance, a neutron is transferred from a deuteron to the target nucleus, leaving the residual system in a state that reveals the properties of the added neutron orbital.

These reactions have played a central role in defining the shell model: by measuring angular distributions and comparing them to reaction theory (e.g., using the distorted wave Born approximation, DWBA), one can extract:

- The orbital angular momentum l of the transferred nucleon (via angular distribution patterns).
- The spectroscopic factor, quantifying the overlap between the initial and final nuclear states.

Transfer reactions are best suited for stable or long-lived nuclei at relatively low energies (5–50 MeV/u), where they benefit from high cross-sections and well-developed theoretical frameworks [20]. However, they become experimentally challenging for short-lived isotopes and high- Z systems, especially where targets cannot be fabricated.

2.3 Knockout Reactions

With the advent of radioactive beam facilities, transfer methods began to be complemented—and in some cases replaced—by nucleon knockout reactions, particularly in inverse kinematics. In a knockout reaction, such as $(A, A-1)$, a high-energy projectile nucleus collides with a light target (e.g., ${}^2\text{Be}$, C, or H), and a single nucleon is suddenly removed from the projectile.

Knockout reactions operate in the sudden approximation: the interaction is fast enough that the removed nucleon doesn't reconfigure its wavefunction during the process. The resulting residual nucleus and its kinematics encode the structural information of the pre-existing configuration.

By measuring the momentum distribution of the residual fragment and comparing it with theoretical predictions (e.g., via the eikonal reaction model or Glauber theory), one obtains:

- The l -value of the knocked-out nucleon (from the width and shape of the distribution).
- The spectroscopic strength, linked to orbital occupancy.

Knockout reactions revolutionized structure studies of exotic nuclei, especially those near the drip lines, by enabling measurements of systems that could only be formed in-flight.

2.4 From Knockout to Quasi-Free Scattering

While both transfer and knockout reactions have yielded profound insights, their selectivity and interpretability face limitations. Transfer reactions are constrained by target availability and are often restricted to stable systems. Knockout reactions, although experimentally versatile, involve complex reaction dynamics with model dependencies that grow in neutron-rich environments and at higher energies.

To transcend these limitations, quasi-free scattering has re-emerged as a uniquely powerful probe. Conceptually close to knockout, but kinematically richer and theoretically cleaner in many regimes, quasi-free scattering reactions like $(e,e'p)$ and $(p,2p)$ offer direct access to the momentum and separation energy of individual nucleons in their initial nuclear orbitals. In high-energy kinematics, and under the impulse approximation, the

scattering process isolates the interaction between the probe and a single nucleon, while the remaining nucleus acts as a spectator.

This progression—from transfer, to knockout, to quasi-free scattering—represents not just an evolution of experimental technique, but a deepening of our ability to map the quantum landscape inside the nucleus, from its shell structure to the underlying many-body correlations.

2.5 Quasi-free Scattering Reactions

2.5.1 Introduction to Quasi-Free Scattering

Quasi-free Scattering (QFS) has emerged as one of the most powerful tools in nuclear physics to probe the single-particle structure and correlations within atomic nuclei. It encompasses a class of reactions in which an incident probe (either an electron or a proton) interacts predominantly with a single nucleon in the nucleus, while the remaining nucleons act as passive spectators. Under kinematic conditions favoring large momentum and energy transfer, and small final-state interactions (FSI), the process can be approximated by the impulse approximation (IA)—a simplification in which the nuclear many-body system is treated as a collection of quasi-free, independent nucleons.

2.5.2 Historical Context and the Electron-Induced Paradigm

The conceptual and experimental foundations of QFS were established in the 1960s, particularly with the pioneering review by Jacob and Maris (1966) [21], which systematized the theoretical framework for electron-induced QFS reactions of the type $(e,e'p)$. In these reactions, a high-energy electron transfers a well-defined amount of momentum and energy to a proton within the target nucleus, which is then ejected and detected in coincidence with the scattered electron. The kinematic constraints of such experiments enable the reconstruction of the missing energy and momentum of the ejected nucleon, which provides a direct spectroscopic window into the bound-state wavefunction.

This formalism was further refined in the 1973 follow-up by the same authors [22], which accounted for distortions in both the incoming and outgoing waves due to the nuclear potential—introducing the Distorted Wave Impulse Approximation (DWIA). These early $(e,e'p)$ experiments, primarily conducted at SLAC and Saclay, provided critical benchmarks for understanding shell structure, spectroscopic factors, and occupancy probabilities, particularly in medium-mass nuclei like ^{16}O and ^{40}Ca . However, the method remained largely confined to stable nuclei due to the limitations in electron beam-target combinations.

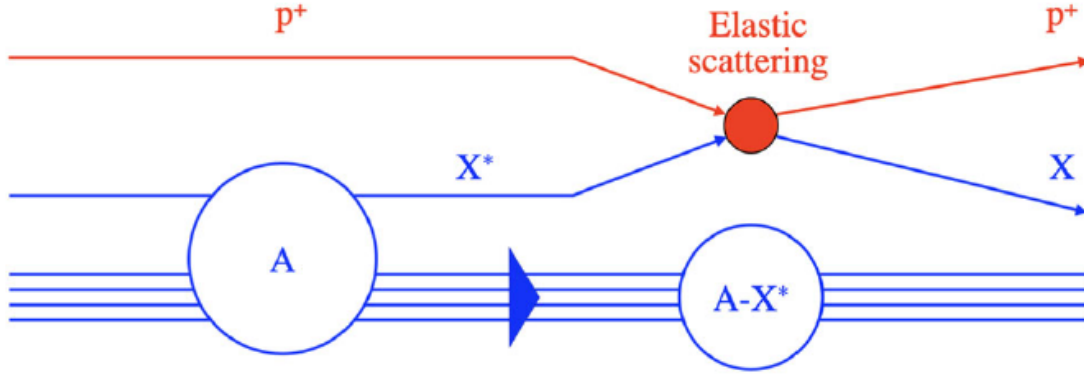


Figure 2.1: Schematic diagram of a QFS reaction induced by a proton p^+ on a nucleus A via elastic scattering off the virtual constituent particle X^* . Three real particles are generated in the final state: the scattered proton p^+ , the knock-out cluster X and the spectator nuclear fragment ($A-X^*$). Reprinted figure from Ref. [24]

2.5.3 Proton-Induced QFS and DWIA Evolution

In parallel, the use of proton-induced QFS—such as $(p,2p)$ or (p,pn) reactions—gained traction as an alternative means to probe the same physics with hadronic probes [23]. While the complexity of the nucleon-nucleon (NN) interaction and stronger final-state interactions initially complicated the analysis, the development of DWIA for hadronic probes enabled the extraction of momentum distributions and spectroscopic observables with comparable reliability. These reactions offered higher cross-sections and better experimental accessibility, though at the cost of increased theoretical uncertainty due to ambiguities in the NN scattering amplitude and optical potentials.

2.5.4 The Modern Era: Inverse Kinematics and Exotic Nuclei

A transformative leap occurred in the 21st century with the advent of inverse kinematics QFS using radioactive ion beams (RIBs) and hydrogen targets. As comprehensively reviewed by Panin et al. (2021) [24], modern QFS experiments at facilities such as RIKEN, GSI/FAIR, and FRIB utilize high-energy beams of neutron- or proton-rich nuclei impinging on proton-rich targets. The resulting reactions—such as $(p,2p)$, (p,pn) , or $(p,p\alpha)$ —enable the study of short-lived and exotic systems far from stability, including halo nuclei, nuclei near the neutron drip line, and those within the so-called "island of inversion."

These experiments exploit complete kinematic reconstruction techniques, coincident γ -ray detection, and high-resolution tracking of all final-state particles. This allows the identification of orbital angular momentum (l) of removed nucleons via momentum distributions, providing a model-independent probe of nuclear shell structure. Moreover, inverse kinematics QFS has facilitated the spectroscopy of unbound states, the quantification of short-range correlations (SRCs) [25–27], and insights into clustering phenomena in

light and medium-mass nuclei [28–30].

2.5.5 Benchmark and Current Frontiers

QFS today occupies a unique position among reaction mechanisms, bridging single-particle and correlated many-body dynamics. Benchmarked by decades of electron-induced QFS data, modern $(p, 2p)/(p, pn)$ measurements are now used to:

- Test shell evolution in neutron-rich isotopes.
- Quantify spectroscopic factors and their reduction (quenching).
- Investigate SRCs in asymmetric nuclear matter.
- Map the extent of the island of inversion.
- Explore the nature of unbound and resonant nuclear states.

Theoretical advancements, notably the eikonal DWIA and relativistic frameworks, allow consistent comparisons between experiment and shell-model or *ab initio* structure predictions. Future developments—such as the integration of machine learning in reaction theory, or the use of polarized beams and targets—promise even finer resolution of nuclear substructure.

EXPERIMENT

"Somewhere, something
incredible is waiting to be
known."

Carl Sagan

3.1 Context and Goal of the Experiment

The proposed experiment, detailed in research proposal G-24-00249 [31], aims to investigate the structure of the neutron-rich fluorine isotope, ^{25}F , through one-proton knockout reactions. This study is motivated by the "drastic extension of the neutron drip line for $Z=9$ compared to $Z=8$ isotopes," a phenomenon that remains poorly understood [32]. The experiment seeks to elucidate how the ^{24}O core is polarized by the presence of an additional proton in ^{25}F , thereby shedding light on the mechanisms responsible for the observed drip line extension.

The experiment will employ the quasi-free scattering (QFS) reaction $^{25}\text{F}(p,2p)^{24}\text{O}$ in inverse kinematics, effectively knocking out a deeply bound valence proton from the ^{25}F nucleus [33]. This approach will utilize the R³B experimental setup, including the high-efficiency neutron detector NeuLAND [34], to achieve complete kinematic measurements and obtain accurate spectroscopic information on the populated final states of ^{24}O . By analyzing the experimental data, researchers aim to determine the extent to which the single $d_{5/2}$ proton in ^{25}F modifies the structure of the core nucleons, potentially indicating deformation or polarization of the ^{24}O core [35].

Ultimately, the goal of this experiment is to provide a more detailed understanding of the nuclear structure of neutron-rich fluorine isotopes and the underlying reasons for the extended neutron drip line at $Z=9$. The results will contribute to a more comprehensive picture of nuclear forces and structure in exotic nuclei, addressing a fundamental question in nuclear physics.

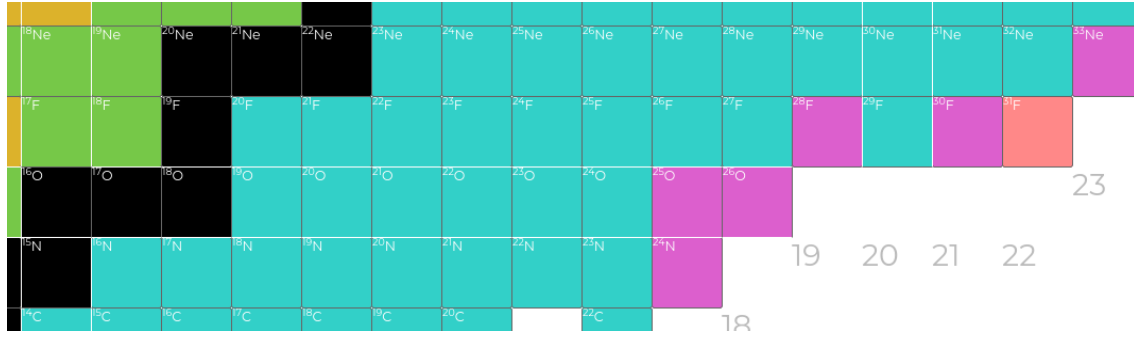


Figure 3.1: Visualization of the neutron drip line extension from oxygen to fluorine. The extended neutron-rich limit for fluorine isotopes illustrates how additional protons influence nuclear binding near the drip line. Figure adapted from the IAEA Live Chart of Nuclides [36].

3.2 The GSI Accelerator System

The previously described experiment will take place at the GSI Helmholtzzentrum für Schwerionenforschung in Darmstadt, Germany. GSI's accelerator complex, seen in Figure 3.2, provides the infrastructure required to produce and deliver rare isotope beams, such as ^{25}F , for inverse kinematics reactions. The R³B setup, located in Cave C downstream of the FRS, enables complete kinematic reconstruction, making it well-suited for the spectroscopic investigation of exotic nuclei. The following sections outline the accelerator chain that delivers these beams—from ion production through the UNILAC and SIS18 to the FRS and the experimental area.

3.2.1 From Source to Experimental Cave

3.2.1.1 Ion Production

The accelerator cycle begins with the production of ions in specialized ion sources. Depending on the experimental requirements, different types of sources are used, including electron cyclotron resonance (ECR) sources and Penning ion sources [38]. These generate high charge state ions by stripping electrons from atoms in a plasma environment. The produced ions are pre-accelerated and then injected into the linear accelerator for further acceleration.

3.2.1.2 The UNILAC

The Universal Linear Accelerator (UNILAC) [39] serves as the primary injector for the GSI accelerator chain. It accelerates ions to energies of several MeV/u before their injection into the synchrotron. Structurally, the UNILAC consists of several stages: a radio-frequency quadrupole (RFQ), an interdigital H-mode drift tube linac (IH-DTL), and a transfer line to the synchrotron SIS18 [40]. Over the years, substantial upgrades have been implemented to accommodate high-intensity beams and improve the beam quality

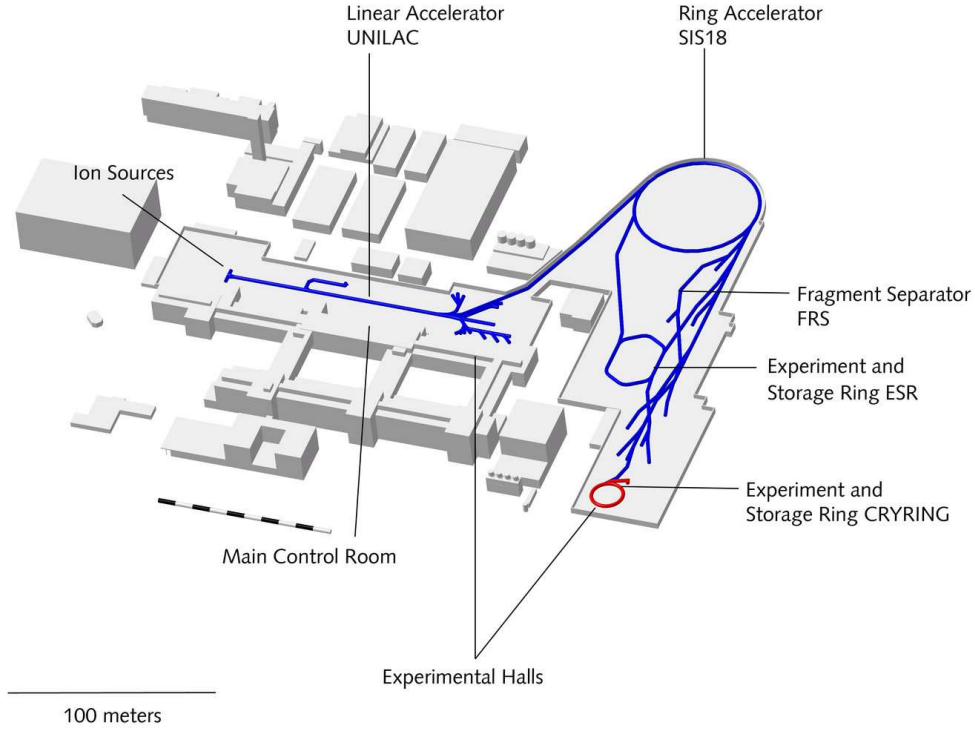


Figure 3.2: Schematic layout of the GSI Helmholtzzentrum accelerator facility. The diagram shows the major components including the ion sources, the UNILAC linear accelerator, the SIS18 synchrotron, the Fragment Separator (FRS), and the associated experimental halls [37].

for heavy ion acceleration . The layout of the UNILAC and its role as the front-end of the accelerator chain is depicted in Figure 3.3.

3.2.1.3 The SIS18

Following pre-acceleration by the UNILAC, ion beams are injected into the SIS18 synchrotron [41], where they are further accelerated to relativistic energies. The SIS18 is a fast-cycling synchrotron with a magnetic rigidity of up to 18 Tm, capable of accelerating ions to several hundred MeV/u. It incorporates sophisticated beam manipulation techniques including bunch compression and multiturn injection to optimize performance and beam delivery. Figure 3.4 illustrates the SIS18 layout and its specifications. The synchrotron serves both as a terminal accelerator for in-house experiments and as an injector for future FAIR components.

3.2.1.4 The Fragment Separator (FRS)

High-energy ions exiting the SIS18 are directed to the FRagment Separator (FRS) [43], a magnetic spectrometer designed for in-flight separation of rare isotopes. The FRS exploits

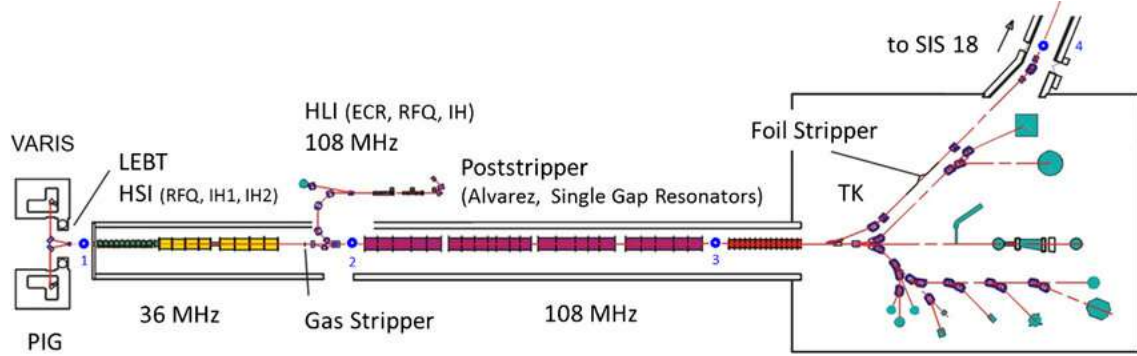


Figure 3.3: Detailed schematic of the UNILAC accelerator. The figure highlights the beamline structure from ion sources through the High Current Injector (HSI), Radio-Frequency Quadrupole (RFQ), Interdigital H-mode Drift Tube Linacs (IH-DTL), gas stripper section, Alvarez Drift Tube Linac (DTL), and the transfer line to SIS18. Beam diagnostic and stripping sections are also labeled [40].

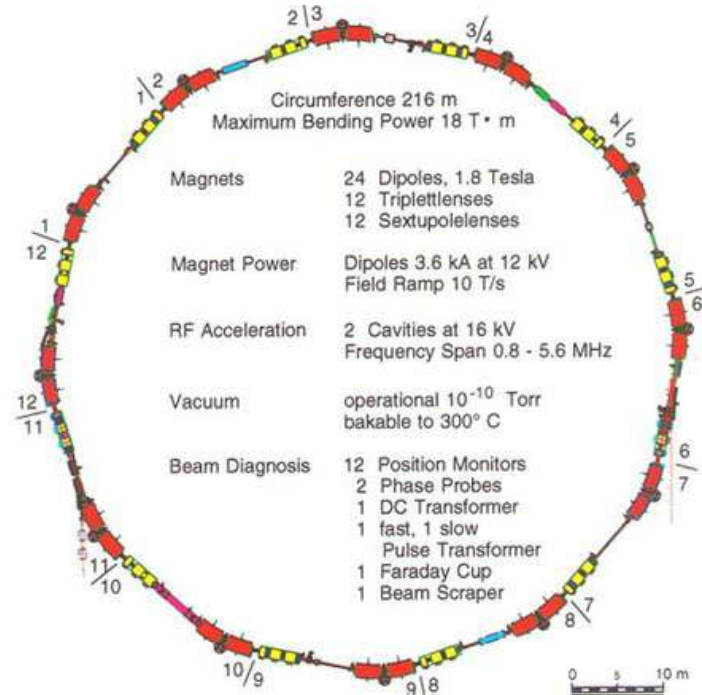


Figure 3.4: Plan view of the SIS18 heavy-ion synchrotron, illustrating its 12 identical lattice sections, dipole and quadrupole magnet configurations, RF acceleration cavities, and positions of beam diagnostic systems [42].

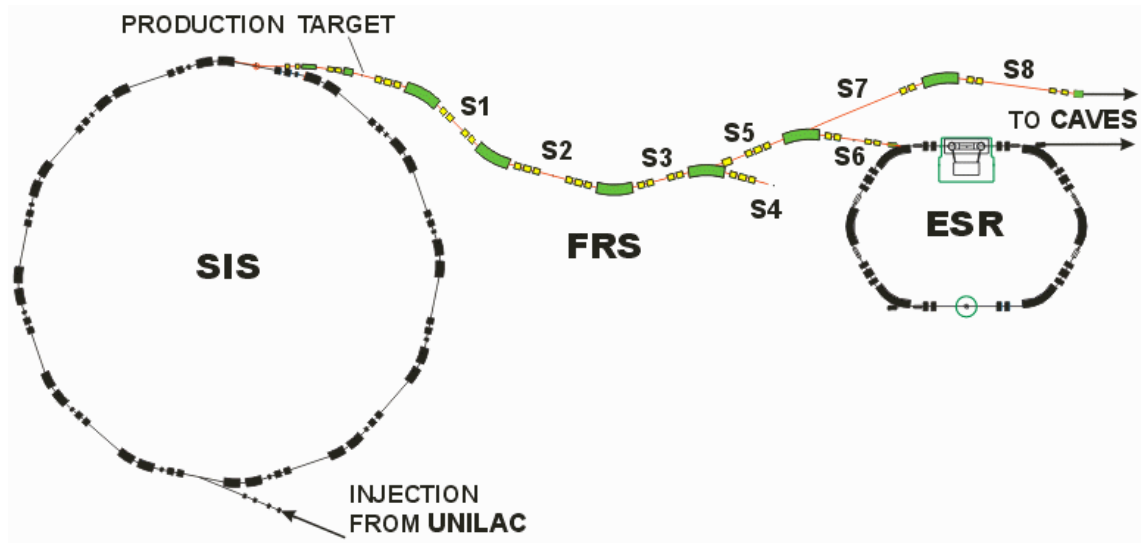


Figure 3.5: Schematic of the FRS system showing its dipole magnet sections, dispersive and achromatic focal planes (F1–F8), and the separation of rare isotope beams. The figure also shows the branching to dedicated experimental areas, including the Direct Branch, Ring Branch (ESR), and the experimental caves [44].

differences in magnetic rigidity and energy loss to isolate specific nuclear species from a cocktail beam. It comprises four dipole magnets forming a two-stage separation system and includes focal planes for tracking, time-of-flight, and energy-loss measurements. As shown in Figure 3.5, the FRS facilitates beam transport from SIS18 to various experimental areas, enabling studies of exotic nuclei and reaction mechanisms.

3.2.1.5 Experimental Caves

Following separation in the FRS, ion beams are directed toward a suite of experimental stations, commonly referred to as experimental caves. These caves are equipped for diverse research programs ranging from nuclear structure and astrophysics to plasma physics and medical applications. One of the principal experimental areas is Cave C, located directly downstream of the FRS. This cave is the one that hosts the R³B setup.

Cave C serves as a prototype environment for the future NUSTAR experiments at FAIR. Specifically, the R³B instrumentation and experimental approach implemented at GSI are being used to develop and validate detector technologies and methodologies for the NUSTAR Cave under construction at FAIR. This strategic continuity ensures a seamless transition of experimental capabilities and scientific objectives from the current GSI facility to the FAIR complex.

The overall layout of the GSI accelerator chain and its future integration with FAIR, including the locations of Cave C and the planned NUSTAR cave, is illustrated in Figure 3.6.

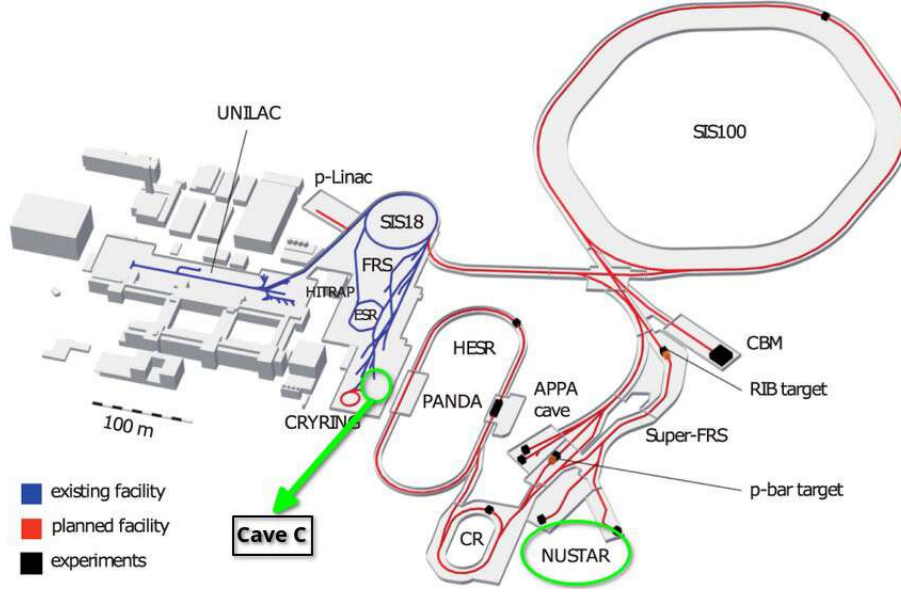


Figure 3.6: Layout of GSI-FAIR with Cave C highlighted, where the prototype of the future NUSTAR R³B setup stands and where the present experiment took place.

3.2.1.6 Summary

The GSI accelerator system exemplifies a complex yet highly coordinated infrastructure, progressing from ion production through successive acceleration stages and culminating in precision experiments. The integration of the UNILAC, SIS18, and FRS ensures the delivery of high-intensity, high-quality ion beams, establishing GSI as a cornerstone of heavy ion research.

3.2.2 Beam used in Experiment

In the proposed experiment [31], a ^{40}Ar primary beam with an energy of 700 MeV/u is employed to produce a secondary beam containing the ^{25}F isotope of interest. The primary beam impinges on a beryllium target located at the FRS, inducing nuclear fragmentation reactions. This process generates a cocktail beam consisting of various isotopes, including ^{25}F , which is then selected and guided towards the experimental setup in Cave C.

The FRS is used to separate and purify the secondary beam, ensuring a sufficient intensity of ^{25}F for the subsequent experiment. As seen in Figure 3.7, LISE++ simulations, using the EPAX3.1a production model, predict an intensity of approximately 30 ions per second (pps) of ^{25}F on the secondary target [31]. The total intensity of the secondary cocktail beam in Cave C is expected to be below 700 pps, with a purity of around 5% for ^{25}F [31]. The relatively low total intensity allows for data acquisition without significant downscaling of triggers and minimizes dead time.

In Cave C, the ^{25}F secondary beam interacts with a liquid hydrogen (LH2) target, which serves as the reaction target for the one-proton knockout reaction $^{25}\text{F}(p,2p)^{24}\text{O}$. The

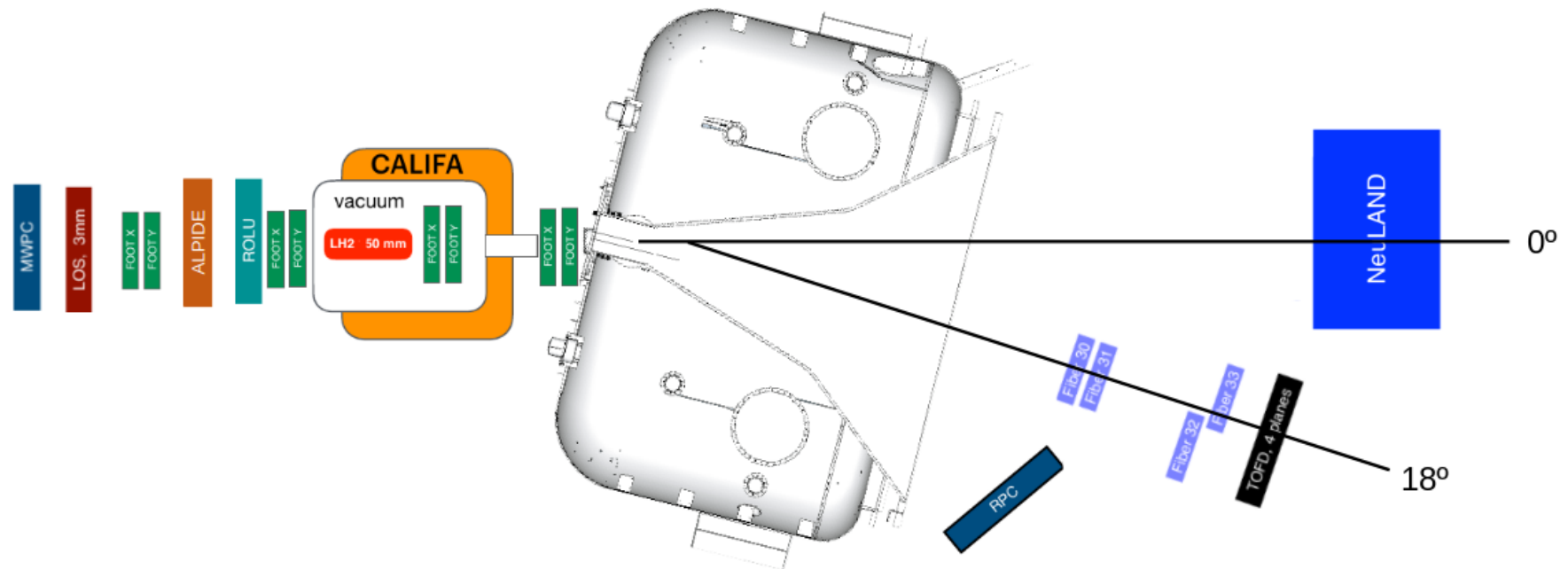
²⁴ Ne	²⁵ Ne	²⁶ Ne	²⁷ Ne	²⁸ Ne	²⁹ Ne
		4.47e-1 0.003%	3.19e+1 2.364%	7.94e+0 8.192%	2.57e-2 0.446%
²³ F	²⁴ F	²⁵ F	²⁶ F	²⁷ F	
1.19e-1 2e-4%	4.12e+1 0.7%	3.1e+1 6.879%	2.86e-1 1.028%	7.93e-6 5.6e-4%	
²² O	²³ O	²⁴ O			
1.04e+2 4.561%	2.21e+0 1.471%	5.14e-4 0.006%			

Figure 3.7: Expected secondary cocktail beam of ^{25}F in Cave C as obtained by LISE++ calculations. The numbers under the names of isotopes indicate calculated rates per second. Reprinted figure from Ref. [31].

LH2 target is positioned in the center of the CALIFA calorimeter, enabling the detection of outgoing protons from the reaction. The use of a 150 mm thick LH2 cell was initially planned but, due to problems in the liquefaction phase, the cell was replaced for a 50 mm one, reducing the reaction yield.

3.3 R³B Setup

The R³B (Reactions with Relativistic Radioactive Beams) setup at GSI is designed for high-precision, kinematically complete measurements of nuclear reactions involving rare isotope beams at relativistic energies. For the investigation of the $^{25}\text{F}(p,2p)^{24}\text{O}$ reaction, the configuration is optimized to detect all relevant particles emerging from the target—charged fragments, recoil protons, and neutrons—with high resolution and full angular coverage. The following description reflects the actual experimental layout, based on the schematic shown in Figure 3.8, and supported by the experimental proposal and detector-specific references.

Figure 3.8: Sketch of the experimental setup at R³B.

3.3.1 Role of each detector

3.3.1.1 Beam Tracking and Initial Identification

The experiment begins with a multi-wire proportional chamber (**MWPC**) placed at the entrance of Cave C. This detector provides coarse spatial information on the incoming secondary beam with minimal material interaction, supporting initial trajectory determination [45].

The **LOS**, positioned directly downstream of the MWPC, serves as the start detector for time-of-flight measurements and provides fast timing and energy-loss signals for particle identification. With a thickness of 3 mm, LOS offers good timing resolution while preserving beam quality [31].

Immediately following LOS, a pair of **FOOTs**—silicon-strip detectors—measure the position and energy loss of incoming ions. These detectors enable fine angular resolution and contribute to charge (Z) identification, enhancing particle-by-particle beam tagging.

3.3.1.2 ALPIDE: High-Precision Pixel Tracking

Downstream of the first FOOT pair, the beam encounters the **ALPIDE** detector. Originally developed for the ALICE ITS upgrade at CERN, ALPIDE is a monolithic active pixel sensor (MAPS) built using the 180 nm CMOS imaging process. Its architecture allows for in-pixel amplification and digitization with very low power consumption (<40 mW/cm²), high spatial resolution (~ 5 μ m), and detection efficiencies exceeding 99% [46].

ALPIDE's design includes a fast, continuously active front-end and in-matrix sparsification, which minimizes data volume by transmitting only hit pixel addresses. This makes it ideal for high-rate tracking applications like R³B. Its placement directly before the target provides excellent vertex resolution when combined with upstream and downstream tracking data.

3.3.1.3 ROLU and Second FOOT Pair

The **ROLU** acts as a beam collimation device, though not in the form of a physical absorber. Instead, it consists of four plastic scintillators arranged to define a square aperture, with the individual scintillators movable to adjust the effective beam window. The system is integrated into the trigger logic: if a particle traverses one of the scintillators, a reject signal is issued and the corresponding event is discarded. Only particles passing cleanly through the defined square aperture—without activating the scintillators—are accepted as valid events. In this way, ROLU effectively performs the role of a beam collimator by suppressing halo particles and defining the accepted beam profile, while relying purely on veto logic rather than material absorption.

Immediately after ROLU is a second pair of FOOT detectors, which reinforces the pre-target tracking and ensures consistent charge and trajectory measurements across multiple stages.

3.3.1.4 Target and CALIFA

The nuclear reaction occurs in a 50 mm liquid hydrogen (LH₂) target, housed in a vacuum chamber and centrally located within the **CALIFA** (CALorimeter for In-Flight particles and γ -rays) detector. CALIFA is composed of CsI(Tl) crystals in a barrel geometry surrounding the target and is designed to detect both recoil protons and γ -rays emitted from excited nuclei. Its energy resolution ($\sim 5\text{--}6\%$ at 1 MeV) and high granularity make it suitable for reconstructing angular distributions and reaction dynamics [47].

3.3.1.5 Post-Target Fragment Tracking

Two additional FOOT pairs are placed downstream of the target: one immediately following the exit window and the other just beyond CALIFA. These silicon-strip detectors provide post-reaction trajectory and Z information for the heavy charged fragments, supporting full momentum reconstruction and enabling vertex association when correlated with upstream tracks.

3.3.1.6 Magnetic Spectrometer: GLAD

The deflection of charged fragments is performed by **GLAD** (GSI Large Acceptance Dipole), a superconducting dipole magnet optimized for large-aperture, high-rigidity measurements. Operated at reduced current for this experiment, GLAD enables separation of oxygen isotopes by their magnetic rigidity, facilitating identification of the reaction residues such as ^{22}O , ^{23}O and ^{24}O .

3.3.1.7 Downstream Branches

After GLAD, the detection branches diverge to accommodate different particle species:

- **Neutron Arm:** Neutrons produced in the decay of unbound states travel undeviated to **NeuLAND**, a high-efficiency detector composed of 3000 plastic scintillator bars. NeuLAND offers sub-150 ps time resolution and spatial precision of ~ 1.5 cm, allowing for accurate time-of-flight measurements and invariant-mass reconstruction in multi-neutron events. It plays a central role in identifying final states like $^{23}\text{O} + n$ and $^{22}\text{O} + 2n$.
- **Fragment Arm:** Charged fragments deflected by GLAD are tracked by four **scintillating fiber detectors**, designated Fiber 30, 31, 32 and 33. These detectors provide fine spatial resolution along the beam axis. Final time-of-flight and charge identification are performed by the **ToFD**, a four-plane plastic scintillator wall with timing precision better than 20 ps and Z resolution sufficient for fragment identification [48].
- **Third Arm:** A **Resistive Plate Chamber (RPC)** is also located in a separate branch downstream of GLAD. While its role in this experiment is limited to specific

measurements, the RPC provides complementary timing and tracking information. A more detailed discussion of the RPC system will follow in the next chapter.

3.3.2 Main DAQ

The R3B experimental setup is integrated through a centralized Data Acquisition (DAQ) system designed to operate in a trigger-coincidence mode across all detectors. Each detector is independently connected to the main DAQ and continuously monitors for signals corresponding to particle interactions. Upon detecting such a signal, a detector issues a trigger request to the central DAQ. When multiple detectors generate simultaneous or time-correlated trigger requests—indicative of a valid physical event—the system recognizes this as a global trigger. In response, the DAQ issues a trigger accept signal, prompting all participating detectors to read out and store the corresponding event data.

The digitized data from each detector are then merged into a single event stream and recorded in a common LMD (List Mode Data) file format. This format preserves the temporal correlation by organizing the information from all subsystems into event-by-event structures. To ensure consistency and temporal alignment across the detector systems, a synchronization signal is distributed at a frequency of approximately 10 Hz. This reference signal provides regular timing markers, allowing for verification and correction of potential timing drifts or misalignments during offline analysis.

3.4 Personal Contribution to the Experiment

"The scientist is not a person who gives the right answers, but one who asks the right questions — and builds the tools to answer them."

Claude Lévi-Strauss
(paraphrased)

4.1 Introduction and Historical Context

Resistive Plate Chambers (RPCs) are gaseous ionization detectors introduced in the early 1980s as a cost-effective solution for large-area charged-particle detection with excellent time resolution. Their working principle relies on the formation of localized electron avalanches in a thin gas gap between two resistive electrodes, typically made of glass or bakelite, under a strong uniform electric field [49]. When a charged particle traverses the gas volume, it ionizes the medium, creating primary electron-ion pairs. The applied electric field accelerates the liberated electrons, initiating an avalanche multiplication process that induces a fast signal on metallic readout strips placed outside the resistive electrodes.

The original single-gap RPC design offered sub-nanosecond timing capabilities and good detection efficiency at relatively low cost, making it widely adopted in high-energy physics experiments. Subsequent developments led to the introduction of Multi-Gap Resistive Plate Chambers (MRPCs), which consist of several narrow gas gaps arranged in parallel between resistive plates [49]. This configuration enhances the detector's timing precision by reducing statistical fluctuations in avalanche development and limiting the overall charge per avalanche, improving rate capability and stability. MRPCs have become the standard in modern time-of-flight (TOF) systems in nuclear and particle physics, delivering intrinsic time resolutions below 50 ps for minimum ionizing particles (MIPs) and efficiencies exceeding 98% [50].

Due to their scalability, robustness, and excellent timing performance, RPCs and MRPCs are extensively employed in experiments at facilities such as CERN, GSI, and RHIC, particularly in large TOF walls and tracking systems. Their application in relativistic heavy-ion collisions, rare-isotope beam experiments, and cosmic-ray detectors demonstrates their versatility and importance in modern experimental physics.

4.2 Detector Design, Construction, and Properties

The Resistive Plate Chamber (Resistive Plate Chamber (RPC)) implemented in the R³B experimental setup at GSI is a large-area timing detector developed for precise identification of charged fragments in relativistic heavy-ion collisions [50]. It is based on the Multi-Gap RPC (MRPC) concept, which significantly enhances timing performance through multiple narrow gas gaps that ensure stable avalanche development.

The detector comprises two identical modules, each hosting a six-gap glass stack, giving a total of twelve 0.3 mm-thick gas gaps per detection plane. These gaps are defined by fishing lines to guarantee uniform separation between the electrodes. The electrodes themselves consist of 1 mm-thick float glass coated with a resistive layer that provides uniform high-voltage distribution. Together, the modules form an active detection area of $1550 \times 1250 \text{ mm}^2$ (1.94 m^2), making this RPC one of the largest deployed in nuclear physics experiments.

The readout system is composed of 41 copper strips, each 29 mm wide and 1600 mm long, arranged on a central PCB placed between the two modules. Each strip is read out on both ends, referred to as the left and right sides. This configuration enables reconstruction of the Y-position from the strip index and the X-position from the signal arrival time difference between both ends. Timing measurements are performed using front-end electronics based on NINO ASICs, which provide fast leading-edge discrimination and time-over-threshold (ToT) encoding. The digitization stage employs TRB boards equipped with multi-channel TDCs featuring sub-30 ps resolution, ensuring precise timing measurements even under high-rate conditions.

The detector operates in avalanche mode with a gas mixture of 98% tetrafluoroethane ($\text{C}_2\text{H}_2\text{F}_4$) and 2% sulfur hexafluoride (SF_6), maintained slightly below atmospheric pressure. The working voltage is approximately 3 kV per gap, resulting in a total applied potential of $\sim 18 \text{ kV}$ per module. This configuration ensures efficient avalanche formation while suppressing streamer transitions and electrical breakdown.

Performance benchmarks obtained in previous tests and beam time campaigns confirm the excellent capabilities of this RPC design. The detector achieves a timing resolution of 50–80 ps for minimum ionizing particles in controlled conditions, and approximately 80–100 ps in realistic beam environments, where additional contributions from reference detectors and beam spread are included. The detection efficiency exceeds 95% under beam conditions and can reach 98% in optimized laboratory setups. Spatial resolution is governed by the 29 mm strip pitch in the vertical direction and the signal propagation

velocity along the strip for the horizontal position, yielding sub-centimeter accuracy in X after calibration [50, 51].

A schematic representation of the detector geometry and strip layout is shown in Figure 4.1.

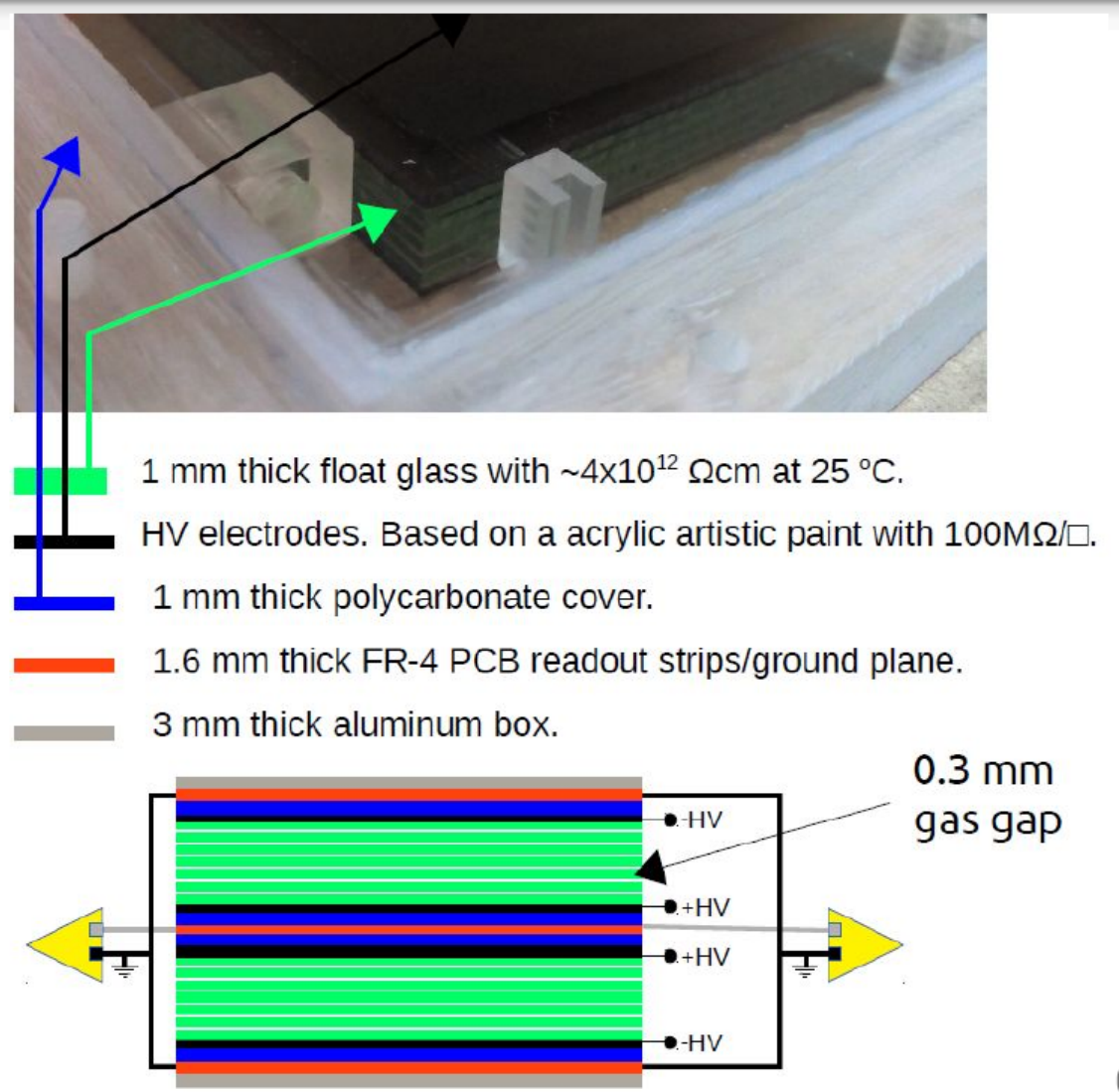


Figure 4.1: Schematic representation of the top view of the RPC. Reprinted from [50].

4.3 Operating Principle and Gas System

4.3.1 Gas Mixture and Physics Motivation

The RPC operates with a carefully selected gas mixture composed of 98% tetrafluoroethane ($\text{C}_2\text{H}_2\text{F}_4$), also known as R-134a or Freon, and 2% sulfur hexafluoride (SF_6). This specific

combination plays a critical role in establishing a stable and efficient ionization environment, ensuring optimal charge amplification and suppression of undesired discharges.

C₂H₂F₄ (Tetrafluoroethane)

As the primary component of the mixture, C₂H₂F₄ serves as the ionization medium and is responsible for supporting electron avalanches. Charged particles traversing the detector ionize the gas, liberating electrons that are accelerated by the applied electric field. Due to its moderate ionization energy (~13.10 eV) [52], C₂H₂F₄ enables efficient impact ionization, resulting in the formation of localized electron avalanches. Its polyatomic molecular structure provides internal vibrational modes that help absorb excess energy, thus preventing the transition to streamer mode. Furthermore, its relatively low electron diffusivity promotes spatially confined signal generation, preserving time resolution and detector stability.

SF₆ (Sulfur Hexafluoride)

Although present in a small fraction, SF₆ is vital to the safe operation of the RPC. As a strongly electronegative gas, SF₆ captures free electrons and suppresses excessive avalanche growth, thus preventing transitions to streamer or breakdown regimes. It also serves as a quenching agent by absorbing ultraviolet photons emitted by excited C₂H₂F₄ molecules, which would otherwise induce secondary avalanches. Through these mechanisms, SF₆ enhances the stability of the avalanche mode and significantly improves timing performance.

4.3.2 Operating Pressure

The internal pressure of the RPC is maintained slightly below atmospheric levels. This configuration is mechanically advantageous, as the higher external atmospheric pressure effectively compresses the detector structure, keeping the glass stacks firmly aligned and minimizing the risk of internal gaps or misalignments.

4.3.3 Detector Operating Modes

The RPC can, in principle, operate in three distinct regimes:

- **Avalanche Mode (Preferred):** The detector operates with controlled charge multiplication, producing fast, localized signals with minimal dead time. The presence of SF₆ is crucial to maintaining operation in this regime.
- **Streamer Mode (Undesired):** Inadequate quenching may lead to excessive avalanche growth and transition to streamer discharges, degrading time and spatial resolution and risking damage to the detector.

- Breakdown Mode (Failure): In the absence of sufficient suppression mechanisms, an uncontrolled discharge may occur, leading to continuous current flow and permanent damage to the detector plates.

The selected gas mixture and voltage operating point are tuned specifically to maintain operation within the avalanche mode, maximizing performance and longevity.

4.4 Readout Electronics and Signal Reconstruction

The RPC detector is read out using a differential system in which each of the signal strips is instrumented on both ends—referred to as the left and right sides. For each event in which a signal crosses a predefined threshold, the readout system records the strip number, the leading and trailing edge times (i.e., the time when the signal crosses the threshold on both the rising and falling edges), and the side (left or right) on which the signal was detected.

From this raw information, a hit can be reconstructed by extracting three key physical quantities: the spatial coordinates of the hit on the detector plane (X and Y), and the time information necessary for further analysis and event building.

- Y-position: The vertical position of the hit is determined directly from the strip number. Each strip has a fixed pitch (in this case, 3 cm), so the position along the Y-axis is given by the centerline of the corresponding strip.
- X-position: The horizontal position along the strip is reconstructed using the time difference between the left and right sides. Assuming a known signal propagation speed along the strip, the hit position is computed from the time asymmetry:

$$X = \frac{1}{2}(t_{right} - t_{left})$$

where t_{right} and t_{left} are the leading edge times on each end. This method assumes uniform propagation speed and symmetric signal shape, which are validated through calibration.

- Time Over Threshold (ToT): The time over threshold is defined as the difference between the trailing and leading edge times for a given signal. It provides an estimate of the pulse height (i.e., deposited charge) and is used as a quality criterion to discriminate valid hits from noise. Only signals with a ToT value within an expected range are accepted for further reconstruction.

This digital processing chain—from raw timing and strip information to physically meaningful hit coordinates—is integrated into the R³B data processing framework. It enables high-resolution tracking and time measurement, critical for associating RPC hits with particle trajectories and for synchronization with the rest of the R³B detector systems.

4.5 Performance in Previous Beam Time

The RPC system underwent its first test during beam time at the R³B setup and demonstrated excellent performance [51]. The detector achieved an efficiency exceeding 95%, with reliable synchronization with the rest of the R³B detectors. The data acquisition was stable over the full two-week operation period, confirming the robustness of both the hardware and software components.

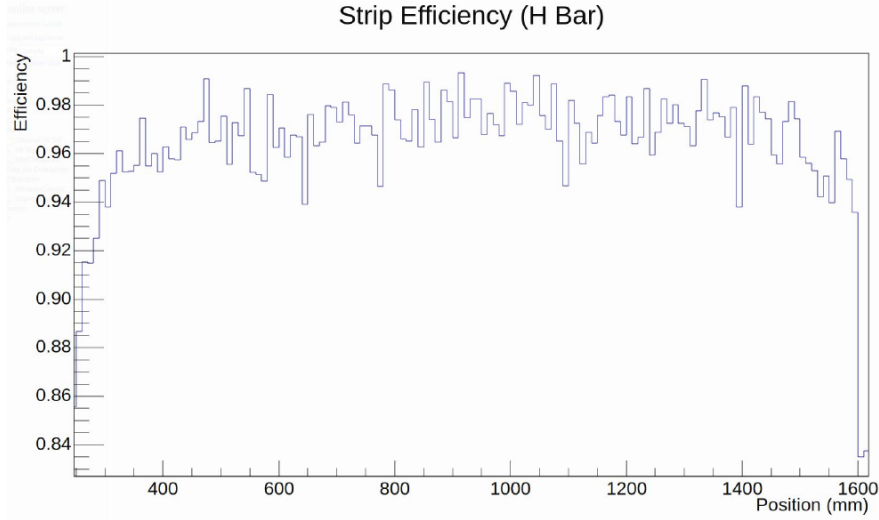


Figure 4.2: Measured strip efficiency of the RPC during beam time.

4.6 Role of the RPC in the Present Experiment

In previous implementations within the R³B experimental setup, the RPC was primarily employed for the detection and timing of protons, operating under well-controlled conditions with relatively low particle multiplicity. The present experiment introduces a new challenge for the detector: the need to process a broader variety of charged particles, including heavier fragments. This scenario represents an important step in validating the RPC technology for more complex experimental conditions, aligning with future applications in FAIR and NUSTAR.

The motivation behind testing the RPC under these conditions lies in assessing its efficiency, timing performance, and overall stability when exposed to an extended particle spectrum beyond protons. Such an evaluation is critical for determining the feasibility of using RPCs as precision timing detectors in high-intensity, high-multiplicity environments, particularly where versatility in particle identification is required.

4.7 Detector Preparation Procedure

The preparation of the RPC prior to beam time involves several carefully controlled steps to ensure proper gas composition, structural stability, and operational calibration:

1. **Drying Phase:** Before filling with the working gas mixture, the RPC is flushed for several days with SF_6 to remove residual moisture. As a more cost-effective alternative, nitrogen was used for this purpose; however, care must be taken to avoid over-pressurization, which could damage the delicate glass structure.
2. **Leak Testing:** Prior to introducing the working gas mixture, the system is tested for leaks. This is done by filling the gas lines while keeping the mass flow controllers closed and monitoring for pressure drops after closing the gas bottles. During this phase, a minor leak was detected. To localize it, various segments of the gas line were isolated and tested independently. These checks did not reveal any leakage in the external tubing, suggesting that the source of the leak was likely located within the RPC chamber itself, or at one of the gas inlet or outlet ports. Despite this issue, the leak was sufficiently small that it did not affect the detector's performance during beam time and did not require immediate intervention.
3. **Gas Insertion and Calibration:** Once leak tightness is confirmed, the 98% $\text{C}_2\text{H}_2\text{F}_4$ / 2% SF_6 gas mixture is introduced. To determine the optimal operating voltage, the detector is calibrated using cosmic ray coincidence measurements. For this purpose, a vertical NeuLAND bar is placed on each side of the RPC. Coincidences allow for the fine adjustment of the high voltage supply to identify the working point that maximizes timing resolution and detection efficiency. An example of these calibration results is presented in Figure ??, which illustrates the dependence of efficiency and signal characteristics on the applied high voltage.

The entire preparation process takes approximately two weeks, after which the detector is ready for integration into the experimental campaign.

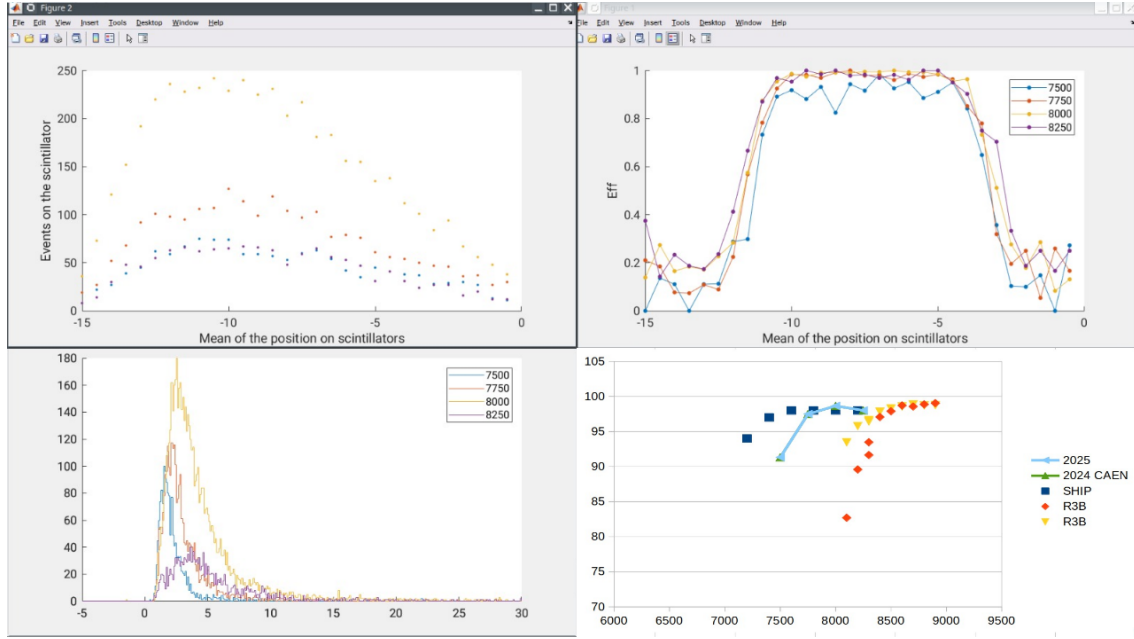


Figure 4.3: Calibration of the RPC working point using cosmic ray data. The top-left panel shows the distribution of events as a function of the mean position on the scintillators for different applied voltages. The top-right panel presents the corresponding efficiency curves as a function of position for four high-voltage settings (7500, 7750, 8000, and 8250 V). The bottom-left panel shows the time-over-threshold (ToT) distributions for the same voltages, which are used as a quality criterion for hit selection. The bottom-right panel summarizes the overall efficiency as a function of the applied voltage, including results from previous beam campaigns for comparison.

4.8 Contributions to Detector Operation and Monitoring

As part of the preparatory and operational phases of the experiment, several tasks related to the control and monitoring of the RPC system were developed or improved. These contributions focused on increasing system reliability, enabling remote intervention, and enhancing real-time observability during beam time.

4.8.1 Monitoring Infrastructure for RPC Voltage and Current

To ensure the stable and safe operation of the RPC, a custom monitoring script was developed to continuously track the voltage and current supplied to the detector's resistive plates. This script interfaces with the high-voltage power supply and records the measured parameters at regular intervals. The collected data are automatically transmitted to a Grafana-based visualization dashboard, providing real-time insights into the detector's electrical behavior. This tool proved essential for diagnosing fluctuations, identifying abnormal conditions during beam time, and maintaining long-term performance stability. These monitoring plots, generated during beam time, are shown in Figure 4.4, where

the stability of the applied voltage and the corresponding current drawn by the resistive plates can be visualized over time.



Figure 4.4: Example of live Grafana dashboard showing voltage and current monitoring of the RPC during beam operation.

4.8.2 Remote Control and Recovery Tools

In addition to monitoring, improvements were made to the RPC control interface by updating and correcting a script used for remote power cycling of the detector. This script also allows for the automated restart of the DAQ and acquisition systems, facilitating rapid recovery in the event of software or hardware issues. These functionalities were used during beam time to reinitialize the RPC without requiring direct physical access to the electronics rack, minimizing downtime and ensuring uninterrupted data collection.

These tools contributed directly to the detector’s robust operation and were successfully integrated into the experimental workflow.

SIMULATION AND ANALYSIS

Whenever there is a problem, it usually lies between the chair and the monitor.

Simulations are a fundamental component of modern nuclear physics experiments, providing a virtual environment where experimental setups, detector responses, and physical processes can be modeled and tested prior to data acquisition. The simulation work in this thesis was conducted using the R3BRoot framework, the dedicated simulation and analysis environment developed for experiments within the R³B collaboration. While R3BRoot was the only framework used directly, it is built upon two widely used and powerful tools in nuclear and high-energy physics: Geant4 and ROOT. It forms a comprehensive framework that enables the design, implementation, analysis, and validation of realistic nuclear experiments. A brief overview of these tools is presented here to provide context for the capabilities offered by R3BRoot.

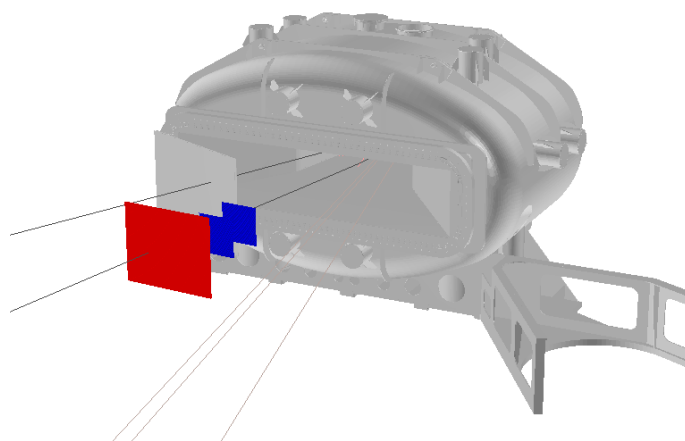


Figure 5.1: Example of an event in a simulation. In this case, there's a ^{14}C passing through ToFD, a Deuteron passing through the RPC and 3 neutrons going to NeuLAND.

5.1 Geant4

Geant4 [53] is a C++ toolkit developed by CERN for simulating the passage of particles through matter. It provides detailed physics models and tracking capabilities that allow for realistic modeling of particle interactions, energy loss, multiple scattering, and nuclear processes. Within R3BRoot, Geant4 is responsible for handling the physical transport of particles through the simulated experimental setup, including interactions with detector materials, magnetic fields, and other components. This embedded use of Geant4 ensures that the simulations reflect the underlying physics of the experiment with high fidelity.

5.2 ROOT

ROOT [54] is an object-oriented data analysis framework that provides tools for statistical analysis, histogramming, visualization, and data storage. R3BRoot integrates ROOT to manage event data, apply reconstruction algorithms, visualize results, and store output in ROOT-compatible formats. ROOT's capabilities are essential for handling the large volumes of simulated data produced and for performing the subsequent analysis and validation steps.

5.3 R3BRoot

R3BRoot [55] is the main framework used throughout this thesis for performing all simulation and analysis tasks. Developed specifically for experiments at the R³B setup, R3BRoot builds on the FairRoot framework [56] and incorporates both Geant4 and ROOT. It provides pre-configured detector geometries, digitization routines, reconstruction algorithms, and analysis tools tailored to the R³B experimental environment.

Using R3BRoot, detailed simulations of the $^{25}\text{F}(p,2p)^{24}\text{O}$ experiment were performed, including particle generation, tracking through the GLAD magnet, propagation through the tracking detectors and the RPC, and emulation of detector responses. The framework also allowed the incorporation of realistic detector resolutions and systematics, enabling the generation of data that closely mirrors what will be observed experimentally. This simulated data formed the basis for developing and validating the Multidimensional Fitting functions presented in this thesis.

5.4 Plots

5.5 Multidimensional Fitting

In experiments like those conducted with the R³B setup, the information directly recorded by detectors is often insufficient on its own to fully reconstruct the physical quantities of interest. Raw observables such as hit positions and times must be interpreted in the context

of the particle's full trajectory, charge, and energy. To bridge this gap, multidimensional fitting (MDF) methods, a procedure of the ROOT framework [57], are used. These tools allow us to model complex, nonlinear relationships between measurable detector signals and the underlying physical properties of particles.

Multidimensional fitting is particularly powerful in the context of quasi-free scattering reactions, such as the one studied in the $^{25}\text{F}(p,2p)^{24}\text{O}$ experiment. Given the diversity and overlap of signals produced by different particles and trajectories in the R^3B setup, MDF enables a more accurate reconstruction of particle kinematics by using correlated detector data. It also allows us to compensate for the intrinsic limitations of individual detectors by combining information from multiple systems.

5.5.1 Application to the RPC and FOOT Detectors

In the simulation phase of this work, MDF techniques were employed to enhance the reconstruction of particle kinematics at the RPC detector — the main focus of this thesis. To train the fitting models, a realistic dataset was generated by simulating the propagation of particles expected to be detected in the experiment, namely protons, alpha particles, deuterons, and ^3He nuclei. These particles were tracked from their production near the target, through the downstream tracking detectors (FOOTs), the GLAD magnet, and finally to the RPC.

Nine input variables were selected to capture the relevant kinematic and spatial information of the particles:

1. The x, y, z positions at the first FOOT detector;
2. The directional angles of the particles (T_x and T_y), calculated from the positions at the first and second FOOTs;
3. The x, y, z positions at the RPC;
4. The time of flight between the last FOOT and the RPC.

These features encapsulate the spatial evolution and timing of the particle along its flight path, providing the necessary information to infer more abstract physical quantities.

Four distinct MDF functions were trained using this dataset:

- A function to estimate the momentum over charge (p/Q) of the particle;
- One function to estimate the momentum in x and another the momentum in y of the particle;
- A function to estimate the flight path (i.e., the actual distance traveled by the particle between the production point and the RPC).

Each function was trained separately to isolate specific aspects of the particle's motion and improve precision. These trained models can later be applied to experimental data to infer momentum and trajectory parameters with higher confidence than would be possible using analytic approximations alone.

This approach demonstrates the importance of data-driven tools like MDF in modern nuclear physics experiments, where complexity and high dimensionality make traditional reconstruction methods insufficient.

5.5.2 Validation of the MDF Models

Once the MDF models were trained, their performance was validated using a new set of Geant4 simulations that modeled a realistic experimental scenario. These simulations incorporated realistic beam-target reactions and included detector resolution effects, reproducing the uncertainties expected in the actual experiment.

For each simulated event, detector observables were extracted and fed into the trained MDF functions, which returned reconstructed values of the physical parameters. These were then compared against the known "true" values from the simulation. The difference between predicted and simulated values was analyzed through a series of performance plots.

The results demonstrated high predictive accuracy of the MDF functions. The residuals between predicted and true values were typically small, with uncertainties reaching down to the order of 10^{-3} in normalized units. This level of precision confirms that the trained functions are robust and reliable, making them suitable for application to real experimental data in the analysis phase.

The successful validation of these MDF models underscores their value as a reconstruction tool in complex experimental setups like R³B. They offer a data-driven approach to extracting meaningful physical insights from otherwise limited detector measurements, playing a central role in the broader simulation and analysis workflow of this thesis.

5.6 Conclusions for the Experiment

RESULTS

This is the results chapter
epigraph.

BIBLIOGRAPHY

- [1] E. Rutherford. "LXXIX. The scattering of α particles by matter and the structure of the atom". en. In: *The London, Edinburgh, and Dublin Philosophical Magazine and Journal of Science* 21.125 (1911-05), pp. 669–688. ISSN: 1941-5982, 1941-5990. DOI: [10.1080/14786440508637080](https://doi.org/10.1080/14786440508637080). URL: <https://www.tandfonline.com/doi/full/10.1080/14786440508637080> (cit. on p. 1).
- [2] C. F. von Weizsacker. "Zur Theorie der Kernmassen". de. In: *Eur. Phys. J. A* 96.7-8 (1935-07), pp. 431–458 (cit. on p. 2).
- [3] H. A. Bethe and R. F. Bacher. "Nuclear Physics A. Stationary States of Nuclei". en. In: *Reviews of Modern Physics* 8.2 (1936-04), pp. 82–229. ISSN: 0034-6861. DOI: [10.1103/RevModPhys.8.82](https://doi.org/10.1103/RevModPhys.8.82). URL: <https://link.aps.org/doi/10.1103/RevModPhys.8.82> (cit. on p. 2).
- [4] M. G. Mayer. "On Closed Shells in Nuclei". In: *Phys. Rev.* 74 (3 1948-08), pp. 235–239. DOI: [10.1103/PhysRev.74.235](https://doi.org/10.1103/PhysRev.74.235). URL: <https://link.aps.org/doi/10.1103/PhysRev.74.235> (cit. on p. 2).
- [5] O. Haxel and J. H. D. Jensen. "On the "Magic Numbers" in Nuclear Structure". en. In: () (cit. on pp. 2, 3).
- [6] M. G. Mayer and J. H. D. Jensen. *Elementary Theory of Nuclear Shell Structure*. Wiley, 1955 (cit. on p. 2).
- [7] W. M. Elsasser. "Sur le principe de Pauli dans les noyaux". fr. In: *Journal de Physique et le Radium* 4.10 (1933), pp. 549–556. ISSN: 0368-3842. DOI: [10.1051/jphysrad:01933004010054900](https://doi.org/10.1051/jphysrad:01933004010054900). URL: <http://www.edpsciences.org/10.1051/jphysrad:01933004010054900> (cit. on p. 2).
- [8] M. G. Mayer, J. Hans, and D. Jensen. "SHELL CLOSURE AND jj COUPLING". en. In: *Alpha-, Beta- and Gamma-Ray Spectroscopy*. Elsevier, 1968, pp. 557–582. ISBN: 978-0-7204-0083-0. DOI: [10.1016/B978-0-7204-0083-0.50020-1](https://doi.org/10.1016/B978-0-7204-0083-0.50020-1). URL: <https://linkinghub.elsevier.com/retrieve/pii/B9780720400830500201> (cit. on p. 2).

- [9] K. S. Krane. *Introductory nuclear physics*. en. Rev. ed., [Nachdr.] Hoboken, NJ: Wiley, 1988. ISBN: 978-0-471-80553-3 (cit. on p. 3).
- [10] T. Otsuka et al. “Evolution of shell structure in exotic nuclei”. en. In: *Reviews of Modern Physics* 92.1 (2020-03), p. 015002. ISSN: 0034-6861, 1539-0756. DOI: [10.1103/RevModPhys.92.015002](https://doi.org/10.1103/RevModPhys.92.015002). URL: <https://link.aps.org/doi/10.1103/RevModPhys.92.015002> (cit. on p. 4).
- [11] P. Spiller et al. “The FAIR Heavy Ion Synchrotron SIS100”. en. In: *Journal of Instrumentation* 15.12 (2020-12), T12013–T12013. ISSN: 1748-0221. DOI: [10.1088/1748-0221/15/12/T12013](https://doi.org/10.1088/1748-0221/15/12/T12013). URL: <https://iopscience.iop.org/article/10.1088/1748-0221/15/12/T12013> (cit. on p. 4).
- [12] M. Winkler et al. “The status of the Super-FRS in-flight facility at FAIR”. en. In: *Nuclear Instruments and Methods in Physics Research Section B: Beam Interactions with Materials and Atoms* 266.19-20 (2008-10), pp. 4183–4187. ISSN: 0168583X. DOI: [10.1016/j.nimb.2008.05.073](https://doi.org/10.1016/j.nimb.2008.05.073). URL: <https://linkinghub.elsevier.com/retrieve/pii/S0168583X08007015> (cit. on p. 4).
- [13] C. Sturm, B. Sharkov, and H. Stöcker. “1, 2, 3 ... FAIR !” en. In: *Nuclear Physics A* 834.1-4 (2010-03), pp. 682c–687c. ISSN: 03759474. DOI: [10.1016/j.nuclphysa.2010.01.124](https://doi.org/10.1016/j.nuclphysa.2010.01.124). URL: <https://linkinghub.elsevier.com/retrieve/pii/S0375947410001259> (cit. on p. 5).
- [14] G. Rosner. “Future Facility: FAIR at GSI”. en. In: *Nuclear Physics B - Proceedings Supplements* 167 (2007-05), pp. 77–81. ISSN: 09205632. DOI: [10.1016/j.nuclphysbps.2006.12.089](https://doi.org/10.1016/j.nuclphysbps.2006.12.089). URL: <https://linkinghub.elsevier.com/retrieve/pii/S0920563206010516> (cit. on p. 5).
- [15] H. Stoecker and C. Sturm. “The FAIR start”. en. In: *Nuclear Physics A* 855.1 (2011-04), pp. 506–509. ISSN: 03759474. DOI: [10.1016/j.nuclphysa.2011.02.117](https://doi.org/10.1016/j.nuclphysa.2011.02.117). URL: <https://linkinghub.elsevier.com/retrieve/pii/S0375947411002041> (cit. on p. 5).
- [16] T. Stöhlker et al. “APPA at FAIR: From fundamental to applied research”. en. In: *Nuclear Instruments and Methods in Physics Research Section B: Beam Interactions with Materials and Atoms* 365 (2015-12), pp. 680–685. ISSN: 0168583X. DOI: [10.1016/j.nimb.2015.07.077](https://doi.org/10.1016/j.nimb.2015.07.077). URL: <https://linkinghub.elsevier.com/retrieve/pii/S0168583X15006552> (cit. on p. 5).
- [17] K. Agarwal. “The Compressed Baryonic Matter (CBM) Experiment at FAIR – Physics, Status and Prospects”. en. In: *Physica Scripta* (2023-02). ISSN: 0031-8949, 1402-4896. DOI: [10.1088/1402-4896/acbca7](https://doi.org/10.1088/1402-4896/acbca7). URL: <https://iopscience.iop.org/article/10.1088/1402-4896/acbca7> (cit. on p. 5).

-
- [18] M. Destefanis. “The PANDA experiment at FAIR”. en. In: *Nuclear Physics B - Proceedings Supplements* 245 (2013-12), pp. 199–206. ISSN: 09205632. DOI: [10.1016/j.nuclphysbps.2013.10.040](https://doi.org/10.1016/j.nuclphysbps.2013.10.040). URL: <https://linkinghub.elsevier.com/retrieve/pii/S0920563213006269> (cit. on p. 5).
 - [19] T. Nilsson and for the NUSTAR collaboration. “The NUSTAR project at FAIR”. en. In: *Physica Scripta* T166 (2015-11), p. 014070. ISSN: 0031-8949, 1402-4896. DOI: [10.1088/0031-8949/2015/T166/014070](https://doi.org/10.1088/0031-8949/2015/T166/014070). URL: <https://iopscience.iop.org/article/10.1088/0031-8949/2015/T166/014070> (cit. on p. 6).
 - [20] G. R. Satchler. *Direct nuclear reactions*. 1983-01 (cit. on p. 8).
 - [21] G. Jacob and T. A. J. Maris. “Quasi-Free Scattering and Nuclear Structure”. en. In: *Reviews of Modern Physics* 38.1 (1966-01), pp. 121–142. ISSN: 0034-6861. DOI: [10.1103/RevModPhys.38.121](https://doi.org/10.1103/RevModPhys.38.121). URL: <https://link.aps.org/doi/10.1103/RevModPhys.38.121> (cit. on p. 9).
 - [22] G. Jacob and T. A. J. Maris. “Quasi-Free Scattering and Nuclear Structure. II.” en. In: *Reviews of Modern Physics* 45.1 (1973-01), pp. 6–21. ISSN: 0034-6861. DOI: [10.1103/RevModPhys.45.6](https://doi.org/10.1103/RevModPhys.45.6). URL: <https://link.aps.org/doi/10.1103/RevModPhys.45.6> (cit. on p. 9).
 - [23] T. Aumann, C. A. Bertulani, and J. Ryckebusch. “Quasifree ($p, 2p$) and (p, pn) reactions with unstable nuclei”. en. In: *Physical Review C* 88.6 (2013-12), p. 064610. ISSN: 0556-2813, 1089-490X. DOI: [10.1103/PhysRevC.88.064610](https://doi.org/10.1103/PhysRevC.88.064610). URL: <https://link.aps.org/doi/10.1103/PhysRevC.88.064610> (cit. on p. 10).
 - [24] V. Panin, T. Aumann, and C. A. Bertulani. “Quasi-free scattering in inverse kinematics as a tool to unveil the structure of nuclei: A tribute to Mahir S. Hussein”. en. In: *The European Physical Journal A* 57.3 (2021-03), p. 103. ISSN: 1434-6001, 1434-601X. DOI: [10.1140/epja/s10050-021-00416-9](https://doi.org/10.1140/epja/s10050-021-00416-9). URL: <https://link.springer.com/10.1140/epja/s10050-021-00416-9> (cit. on p. 10).
 - [25] O. Hen et al. “Nucleon-nucleon correlations, short-lived excitations, and the quarks within”. en. In: *Reviews of Modern Physics* 89.4 (2017-11), p. 045002. ISSN: 0034-6861, 1539-0756. DOI: [10.1103/RevModPhys.89.045002](https://doi.org/10.1103/RevModPhys.89.045002). URL: <https://link.aps.org/doi/10.1103/RevModPhys.89.045002> (cit. on p. 10).
 - [26] M. Duer et al. “Direct Observation of Proton-Neutron Short-Range Correlation Dominance in Heavy Nuclei”. en. In: *Physical Review Letters* 122.17 (2019-05), p. 172502. ISSN: 0031-9007, 1079-7114. DOI: [10.1103/PhysRevLett.122.172502](https://doi.org/10.1103/PhysRevLett.122.172502). URL: <https://link.aps.org/doi/10.1103/PhysRevLett.122.172502> (cit. on p. 10).
 - [27] A. Schmidt et al. “Probing the core of the strong nuclear interaction”. en. In: *Nature* 578.7796 (2020-02), pp. 540–544. ISSN: 0028-0836, 1476-4687. DOI: [10.1038/s41586-020-2021-6](https://doi.org/10.1038/s41586-020-2021-6). URL: <https://www.nature.com/articles/s41586-020-2021-6> (cit. on p. 10).

- [28] F. M. Marqués et al. “Detection of neutron clusters”. en. In: *Physical Review C* 65.4 (2002-04), p. 044006. ISSN: 0556-2813, 1089-490X. DOI: [10.1103/PhysRevC.65.044006](https://doi.org/10.1103/PhysRevC.65.044006). URL: <https://link.aps.org/doi/10.1103/PhysRevC.65.044006> (cit. on p. 11).
- [29] F. M. Marqués and J. Carbonell. “The quest for light multineutron systems”. en. In: *The European Physical Journal A* 57.3 (2021-03), p. 105. ISSN: 1434-6001, 1434-601X. DOI: [10.1140/epja/s10050-021-00417-8](https://doi.org/10.1140/epja/s10050-021-00417-8). URL: <https://link.springer.com/10.1140/epja/s10050-021-00417-8> (cit. on p. 11).
- [30] M. Duer et al. “Observation of a correlated free four-neutron system”. en. In: *Nature* 606.7915 (2022-06), pp. 678–682. ISSN: 0028-0836, 1476-4687. DOI: [10.1038/s41586-022-04827-6](https://doi.org/10.1038/s41586-022-04827-6). URL: <https://www.nature.com/articles/s41586-022-04827-6> (cit. on p. 11).
- [31] V. Panin et al. “Unveiling the structure of neutron-rich $Z=9$ isotopes: the case of ^{25}F ”. Unpublished research proposal submitted to GSI Helmholtzzentrum für Schwerionenforschung. 2024 (cit. on pp. 12, 17, 18, 20).
- [32] D. S. Ahn et al. “Location of the Neutron Dripline at Fluorine and Neon”. en. In: *Physical Review Letters* 123.21 (2019-11), p. 212501. ISSN: 0031-9007, 1079-7114. DOI: [10.1103/PhysRevLett.123.212501](https://doi.org/10.1103/PhysRevLett.123.212501). URL: <https://link.aps.org/doi/10.1103/PhysRevLett.123.212501> (cit. on p. 12).
- [33] V. Panin et al. “Exclusive measurements of quasi-free proton scattering reactions in inverse and complete kinematics”. en. In: *Physics Letters B* 753 (2016-02), pp. 204–210. ISSN: 03702693. DOI: [10.1016/j.physletb.2015.11.082](https://doi.org/10.1016/j.physletb.2015.11.082). URL: <https://linkinghub.elsevier.com/retrieve/pii/S0370269315009612> (cit. on p. 12).
- [34] K. Boretzky et al. “NeuLAND: The high-resolution neutron time-of-flight spectrometer for R3B at FAIR”. en. In: *Nuclear Instruments and Methods in Physics Research Section A: Accelerators, Spectrometers, Detectors and Associated Equipment* 1014 (2021-10), p. 165701. ISSN: 01689002. DOI: [10.1016/j.nima.2021.165701](https://doi.org/10.1016/j.nima.2021.165701). URL: <https://linkinghub.elsevier.com/retrieve/pii/S0168900221006860> (cit. on p. 12).
- [35] A. O. Macchiavelli et al. “Core of F^{25} in the rotational model”. en. In: *Physical Review C* 102.4 (2020-10), p. 041301. ISSN: 2469-9985, 2469-9993. DOI: [10.1103/PhysRevC.102.041301](https://doi.org/10.1103/PhysRevC.102.041301). URL: <https://link.aps.org/doi/10.1103/PhysRevC.102.041301> (cit. on p. 12).
- [36] International Atomic Energy Agency. *IAEA Nuclear Data Services: Live Chart of Nuclides*. Accessed: 2025-07-30. 2025. URL: <https://www-nds.iaea.org/relnsd/vcharthtml/VChartHTML.html> (cit. on p. 13).
- [37] GSI Helmholtzzentrum für Schwerionenforschung GmbH. *Accelerator Facility — gsi.de*. https://www.gsi.de/en/researchaccelerators/accelerator_facility. [Accessed 16-05-2025] (cit. on p. 14).

-
- [38] R. Hollinger et al. "Status of high current ion source operation at the GSI accelerator facility". en. In: *Review of Scientific Instruments* 79.2 (2008-02), p. 02C703. ISSN: 0034-6748, 1089-7623. DOI: [10.1063/1.2801623](https://doi.org/10.1063/1.2801623). URL: <https://pubs.aip.org/rsi/article/79/2/02C703/1068369/Status-of-high-current-ion-source-operation-at-the> (cit. on p. 13).
 - [39] H. Vormann et al. "High current heavy ion beam investigations at GSI-UNILAC". en. In: *Journal of Physics: Conference Series* 2420.1 (2023-01), p. 012037. ISSN: 1742-6588, 1742-6596. DOI: [10.1088/1742-6596/2420/1/012037](https://doi.org/10.1088/1742-6596/2420/1/012037). URL: <https://iopscience.iop.org/article/10.1088/1742-6596/2420/1/012037> (cit. on p. 13).
 - [40] W. Barth et al. "High brilliance beam investigations at the universal linear accelerator". en. In: *Physical Review Accelerators and Beams* 25.4 (2022-04), p. 040101. ISSN: 2469-9888. DOI: [10.1103/PhysRevAccelBeams.25.040101](https://doi.org/10.1103/PhysRevAccelBeams.25.040101). URL: <https://link.aps.org/doi/10.1103/PhysRevAccelBeams.25.040101> (cit. on pp. 13, 15).
 - [41] R. Singh. "Tune measurement at GSI SIS-18: Methods and applications". In: (2014) (cit. on p. 14).
 - [42] GSI Helmholtzzentrum für Schwerionenforschung GmbH. *SIS18 Sections* — [gsi.de. https://www.gsi.de/en/work/accelerator_operations/accelerators/heavy_ion_synchrotron_sis18/sis18_sections](https://www.gsi.de/en/work/accelerator_operations/accelerators/heavy_ion_synchrotron_sis18/sis18_sections). [Accessed 16-05-2025] (cit. on p. 15).
 - [43] H. Geissel and Y. A. Litvinov. "Experiments with the FRS facility at GSI". en. In: *Nuclear Instruments and Methods in Physics Research Section B: Beam Interactions with Materials and Atoms* 266.19-20 (2008-10), pp. 4176–4182. ISSN: 0168583X. DOI: [10.1016/j.nimb.2008.05.093](https://doi.org/10.1016/j.nimb.2008.05.093). URL: <https://linkinghub.elsevier.com/retrieve/pii/S0168583X08007003> (cit. on p. 14).
 - [44] GSI Helmholtzzentrum für Schwerionenforschung GmbH. *WebHome < FRS < GSI Wiki* — [wiki.gsi.de. https://wiki.gsi.de/FRS/](https://wiki.gsi.de/FRS/). [Accessed 16-05-2025] (cit. on p. 16).
 - [45] S. Paschalis et al. "The in-beam tracking detectors of the R³B experiment". en. In: (2015). Medium: Abstract Publisher: GSI Helmholtzzentrum fuer Schwerionenforschung, Darmstadt. DOI: [10.15120/GR-2015-1-MU-NUSTAR-NR-15](https://doi.org/10.15120/GR-2015-1-MU-NUSTAR-NR-15). URL: <https://repository.gsi.de/record/183947> (cit. on p. 20).
 - [46] M. Mager. "ALPIDE, the Monolithic Active Pixel Sensor for the ALICE ITS upgrade". en. In: *Nuclear Instruments and Methods in Physics Research Section A: Accelerators, Spectrometers, Detectors and Associated Equipment* 824 (2016-07), pp. 434–438. ISSN: 01689002. DOI: [10.1016/j.nima.2015.09.057](https://doi.org/10.1016/j.nima.2015.09.057). URL: <https://linkinghub.elsevier.com/retrieve/pii/S0168900215011122> (cit. on p. 20).

- [47] D. Cortina-Gil et al. “CALIFA, a Dedicated Calorimeter for the R3B/FAIR”. en. In: *Nuclear Data Sheets* 120 (2014-06), pp. 99–101. ISSN: 00903752. DOI: [10.1016/j.nds.2014.07.017](https://doi.org/10.1016/j.nds.2014.07.017). URL: <https://linkinghub.elsevier.com/retrieve/pii/S0090375214004694> (cit. on p. 21).
- [48] M. Heil et al. “A new Time-of-flight detector for the R³B setup”. en. In: *The European Physical Journal A* 58.12 (2022-12), p. 248. ISSN: 1434-601X. DOI: [10.1140/epja/s10050-022-00875-8](https://doi.org/10.1140/epja/s10050-022-00875-8). URL: <https://link.springer.com/10.1140/epja/s10050-022-00875-8> (cit. on p. 21).
- [49] W. Riegler and C. Lippmann. “The physics of Resistive Plate Chambers”. en. In: *Nuclear Instruments and Methods in Physics Research Section A: Accelerators, Spectrometers, Detectors and Associated Equipment* 518.1-2 (2004-02), pp. 86–90. ISSN: 01689002. DOI: [10.1016/j.nima.2003.10.031](https://doi.org/10.1016/j.nima.2003.10.031). URL: <https://linkinghub.elsevier.com/retrieve/pii/S0168900203027311> (visited on 2025-08-28) (cit. on p. 23).
- [50] A. Blanco et al. “The SHiP timing detector based on MRPC”. en. In: *Journal of Instrumentation* 15.10 (2020-10), pp. C10017–C10017. ISSN: 1748-0221. DOI: [10.1088/1748-0221/15/10/C10017](https://doi.org/10.1088/1748-0221/15/10/C10017). URL: <https://iopscience.iop.org/article/10.1088/1748-0221/15/10/C10017> (visited on 2025-08-22) (cit. on pp. 23–25).
- [51] M. Xarepe et al. “Resistive plate chambers for precise measurement of high-momentum protons in short range correlations at R³B”. en. In: *Nuclear Instruments and Methods in Physics Research Section A: Accelerators, Spectrometers, Detectors and Associated Equipment* 1055 (2023-10), p. 168445. ISSN: 01689002. DOI: [10.1016/j.nima.2023.168445](https://doi.org/10.1016/j.nima.2023.168445). URL: <https://linkinghub.elsevier.com/retrieve/pii/S0168900223004357> (cit. on pp. 25, 28).
- [52] J. Pereira-da-Silva et al. “Electron Driven Reactions in Tetrafluoroethane: Positive and Negative Ion Formation”. en. In: *Journal of the American Society for Mass Spectrometry* 32.6 (2021-06). Publisher: American Chemical Society (ACS), pp. 1459–1468. ISSN: 1044-0305, 1879-1123. DOI: [10.1021/jasms.1c00057](https://doi.org/10.1021/jasms.1c00057). URL: <https://pubs.acs.org/doi/10.1021/jasms.1c00057> (visited on 2025-07-29) (cit. on p. 26).
- [53] S. Agostinelli et al. “Geant4—a simulation toolkit”. en. In: *Nuclear Instruments and Methods in Physics Research Section A: Accelerators, Spectrometers, Detectors and Associated Equipment* 506.3 (2003-07), pp. 250–303. ISSN: 01689002. DOI: [10.1016/S0168-9002\(03\)01368-8](https://doi.org/10.1016/S0168-9002(03)01368-8). URL: <https://linkinghub.elsevier.com/retrieve/pii/S0168900203013688> (cit. on p. 33).
- [54] R. Brun and F. Rademakers. “ROOT — An object oriented data analysis framework”. en. In: *Nuclear Instruments and Methods in Physics Research Section A: Accelerators, Spectrometers, Detectors and Associated Equipment* 389.1-2 (1997-04), pp. 81–86. ISSN: 01689002. DOI: [10.1016/S0168-9002\(97\)00048-X](https://doi.org/10.1016/S0168-9002(97)00048-X). URL: <https://linkinghub.elsevier.com/retrieve/pii/S016890029700048X> (cit. on p. 33).

- [55] D. Bertini. “R3BRoot, simulation and analysis framework for the R3B experiment at FAIR”. en. In: *Journal of Physics: Conference Series* 331.3 (2011-12), p. 032036. ISSN: 1742-6596. DOI: [10.1088/1742-6596/331/3/032036](https://doi.org/10.1088/1742-6596/331/3/032036). URL: <https://iopscience.iop.org/article/10.1088/1742-6596/331/3/032036> (cit. on p. 33).
- [56] M. Al-Turany et al. “The FairRoot framework”. en. In: *Journal of Physics: Conference Series* 396.2 (2012-12). Publisher: IOP Publishing, p. 022001. ISSN: 1742-6588, 1742-6596. DOI: [10.1088/1742-6596/396/2/022001](https://doi.org/10.1088/1742-6596/396/2/022001). URL: <https://iopscience.iop.org/article/10.1088/1742-6596/396/2/022001> (visited on 2025-07-29) (cit. on p. 33).
- [57] ROOT: TMultiDimFit Class Reference. URL: <https://root.cern.ch/doc/master/classTMultiDimFit.html> (visited on 2025-07-29) (cit. on p. 34).

A

RPC PLOTS

GSI ACCELERATOR FACILITY

